Professorship of Lunar and Planetary Exploration
TUM School of Engineering and Design
Technical University of Munich

Design and Analysis of a Cold Plate and Thermal Shroud for a Dirty Thermal-Vacuum Chamber

Engineering Documentation

Omar Elsherbiny

Submitted in partial fulfilment of the requirements for the attainment of the academic degree

Master of Science (M.Sc.)

at the TUM School of Engineering and Design of the Technical University of Munich.

Examiner:
Prof. Dr. Philipp Reiss
Professorship of Lunar and Planetary Exploration

Supervisor:
Rok Sesko
Professorship of Lunar and Planetary Exploration

Submitted:
Munich, 20.04.2024

Declaration of Academic Honesty

I declare that I will use all facilities, equipment, devices and programs made available to me by the Technical University of Munich or by the Professorship of Lunar and Planetary Exploration within the scope of this thesis, project, paper, or internship work in accordance with the intended purpose, the valid guidelines, user regulations or instructions for use and, as far as necessary, only after having received instruction and with all due care. In particular, I will neither copy programs without special instruction from the supervisor nor use them for purposes other than those intended for my work at the professorship. I will not pass on to third parties any information, documents or findings that I have been told are confidential, either during or after my work at the professorship.

I also agree that my thesis may be made available by the professorship to interested persons upon request, also via a library, and that the results contained therein as well as developments and programs resulting therefrom may be used by the Professorship of Lunar and Planetary Exploration without restriction. Rights to any programs and inventions that may arise must be clarified in advance.

I also declare that I have prepared this document without outside help and have only used the sources and aids listed in the bibliography.

Munich, 20.04.2024 Omar Elsherbiny

Omar ElSherbiny

This page was intentionally left blank

Abstract

Experimental setups involving planetary regolith and thermal cycling demand precise thermal control in vacuum conditions. This work introduces a cold plate and thermal shroud system tailored for such conditions in a dusty thermal vacuum chamber at the Technical University of Munich. The design prioritizes compatibility with regolith-based experiments and passive thermal management to maximize available space for experiments while minimizing complexity and contamination risk.

The cold plate was evaluated for its ability to cool a regolith bed first using LN2 then using closed-loop circulation of HFE-7100, a non-conductive coolant. HFE-7100 was selected over liquid nitrogen for its operational flexibility and economical viability. Several cold plate configurations were evaluated, including embedded tube and vacuum brazed designs. Thermohydraulic analysis favored a dual-leg brazed plate geometry for its significantly lower pressure drop, though cost constraints led to the retention of the legacy plate for the current phase.

In parallel, a modular thermal shroud was developed using high-reflectivity 1000-series aluminum and PTFE insulation spacers. Through simulation of multiple configurations, a modified milti-layer design was selected to optimize radiative shielding while preserving experimental space. The design uses modular panel that are interchangeable in specific regions of the chamber. Then integration addressed mechanical constraints, fluid routing, and thermal decoupling strategies to ensure clean operation and future adaptability.

Together, these components form a robust thermal control system that enables repeated use in a contaminated vacuum environment, paving the way for accurate simulation of lunar surface conditions and supporting the upcoming Rover Permittivity Sensor campaign.

Contents

List of Tables

List of Figures

Acronyms

C

CAD - Computer-Aided Design ix, 15, 35

COMSOL - COMSOL Multiphysics 29, 44

E

ESA - European Space Agency 7

F

FSW - Friction Stir Welded 20, 26

H

HFE-7100 - Hydrofluoroether 7100 viii, 16, 17, 20, 21, 26, 29

I

ISO - International Organization for Standardization vii, 4

L

LISA - Lightweight Inter-Satellite Link Antenna viii, 9, 11, 13–15, 43

LN2 - Liquid Nitrogen 16

LPE - Lunar and Planetary Exploration 1, 9

M

MLI - Multi-Layer Insulation 13

P

PEEK - Polyether Ether Ketone 29

PTFE - Polytetrafluoroethylene 25, 29

R

RPS - Rover Permittivity Sensor 14, 15, 43, 44

T

TUM - Technical University of Munich 1, 9, 44

TVAC - Thermal Vacuum Chamber 1, 6, 7, 9

List of Symbols

Symbol	Description	Unit
ρ	Fluid density	kg/m^3
v	Velocity	m/s
Q	Volumetric flow rate	m^3/s
A	Cross-sectional area	m^2
ΔP	Pressure drop	Pa
L	Pipe or flow length	m
D	Hydraulic diameter	m
$\dot{q}$	Heat flux	W/m^2
T	Temperature	K or ℃
k	Thermal conductivity	W/m·K
α	Thermal diffusivity	mm^2/s
K	Minor loss coefficient	–
σ	Stefan–Boltzmann constant	W/m^2·K^4
$F_{i,j}$	View factor from i to j	–
ε	Emissivity	–
ϕ	Radiative heat flux	W
R_{th}	Thermal resistance	K/W
P	Pressure	Pa or bar
h	Heat transfer coefficient	W/m^2·K

1 Introduction

TVACs (Thermal Vacuum Chambers) are essential to the development of spacecraft and planetary exploration technologies. They allow for the environmental testing and qualification of spacecraft and satellite subsystems. This includes thermal testing in a vacuum environment that accurately replicates orbital or planetary conditions. In such environments, conduction and convection from ambient gases are effectively absent, making radiative heat transfer the dominant mode of energy exchange. *TVACs* are therefore used to simulate space-like conditions on the ground and are equipped with radiative enclosures, known as thermal shrouds, that define the thermal boundary conditions around the test specimen.

A thermal shroud is an actively or passively controlled surface that surrounds the experiment or testing equipment and either absorbs or emits radiation to achieve a defined thermal environment. These shrouds must be capable of uniformly distributing heat or cold via radiative means and, depending on the chamber architecture, may need to operate in both heating or cooling modes. The internal surface is usually coated with a reflective layer or with high-emissivity black paint to promote radiative coupling, while temperature control is typically achieved via embedded fluid lines carrying cryogenic or heated gases, though passive methods also exist.

This work was carried out as part of a research internship at the Chair of *LPE (Lunar and Planetary Exploration)* at the *TUM (Technical University of Munich)* and aims to develop a thermal shroud for a small-scale thermal vacuum chamber housed at the *TUM* facilities in Ottobrunn. The goal is to design and analyze a cold plate and thermal shroud for a dirty thermal-vacuum chamber, and to do so using a passive shroud, therefore pushing the limits of passive cooling.

The project covers the full design process, from background research and definition of system requirements to conceptual development, thermal analysis, mechanical design, and integration planning. The resulting thermal shroud should be suitable for repeated use and compatible with experiments that involves the use of regolith simulant. The final design also takes into account material selection, manufacturing feasibility, and long-term operational considerations.

2 Background

2.1 Heat Transfer Mechanisms in Vacuum Environments

In terrestrial environments, thermal energy is transported through three principal mechanisms: conduction, convection, and radiation. However, in vacuum conditions, convection is entirely suppressed due to the absence of a fluid medium. Therefore, only conduction through solid interfaces and radiation between surfaces remain as effective modes of heat transfer. These mechanisms become particularly significant in the design and operation of spacecraft and thermal vacuum test systems.

Thermal conduction refers to the transfer of energy at the microscopic level as particles exchange kinetic energy due to a temperature gradient. In solid materials, especially metals, this energy transport is facilitated primarily by free electrons and lattice vibrations (phonons). For systems in a vacuum, conductive heat transfer occurs strictly through solid mechanical interfaces.

The heat flux due to one-dimensional steady-state conduction is given by Fourier's law (Incropera et al., 2007):

$$\dot{q}_x = -k\frac{dT}{dx} \tag{2.1}$$

where $\dot{q}_x$ is the heat flux density (W/m^2), k is the thermal conductivity of the material (W/m·K), and dT/dx is the temperature gradient along the direction of heat flow.

Assuming a planar wall of thickness x and cross-sectional area A, the total heat transfer rate becomes (Incropera et al., 2007):

$$\dot{Q}_{\text{cond}} = -\frac{k \cdot A}{x} \cdot \Delta T \tag{2.2}$$

This formulation assumes constant material properties and no internal heat generation. In practice, contact resistances at material interfaces must also be considered, particularly in bolted or mechanically fastened assemblies (Incropera et al., 2007).

Thermal radiation is the emission of electromagnetic waves from the surface of a body as a result of its temperature. Unlike conduction and convection, radiation does not require a medium and can propagate across a vacuum. This makes it the dominant heat transfer mechanism between separated surfaces in space or in thermally evacuated environments.

The net radiative heat exchange between two diffuse, grey surfaces can be described using the Stefan–Boltzmann law (Modest, 2013):

$$\dot{Q}_{\text{rad},12} = \varepsilon_1 \cdot \alpha_2 \cdot F_{1\to 2} \cdot A_1 \cdot \sigma \cdot \left(T_1^4 - T_2^4\right) \tag{2.3}$$

where:

- ε_1 is the emissivity of surface 1,
- α_2 is the absorptivity of surface 2,
- $F_{1\to 2}$ is the view factor from surface 1 to surface 2,
- A_1 is the surface area of body 1 (m^2),
- σ is the Stefan–Boltzmann constant (5.670×10^{-8} W/m^2·K^4),
- T_1 and T_2 are the absolute temperatures of the surfaces (K).

The view factor $F_{1\to 2}$ quantifies the geometric relationship between the two surfaces and defines the fraction of energy leaving surface 1 that directly impinges on surface 2. The view factor satisfies reciprocity and enclosure relations such as (Modest, 2013):

$$A_1 F_{1\to 2} = A_2 F_{2\to 1}, \quad \sum_j F_{i\to j} = 1 \tag{2.4}$$

For space applications, surfaces are commonly treated as *grey bodies*, in which the absorptivity and emissivity are constant over the relevant wavelength range. According to Kirchhoff's law, these properties are equivalent for thermodynamic equilibrium (Modest, 2013):

$$\varepsilon_\lambda = \alpha_\lambda \tag{2.5}$$

In thermal vacuum testing, it is often useful to adopt a *semi-grey body* approximation, where surface optical properties are split between shortwave (solar) and longwave (infrared) bands. Thus, separate values α_{sol} and ε_{IR} are defined for absorbed solar radiation and emitted infrared radiation, respectively (Gilmore, 2002a).

Holkeboer et al. (1966) observed that, for accurate simulation of deep-space conditions, radiative exchange must dominate, and any residual gas conduction must be kept minimal. In other words, they determined that pressures below approximately 1.3×10^{-3} Pa (or 10^{-5} Torr) are required to sufficiently suppress conductive heat transfer in gases and somewhat replicate space conditions.

Radiative control in a vacuum is thus central to thermal analysis and test strategies, especially for components undergoing thermal balance testing or orbital thermal cycling profiles, and so material selection, specifically optical properties play a tremendous role in successfully developing a shroud system.

2.2 Vacuum Physics and Gas Dynamics at Low Pressure

Vacuum technology plays an essential role in the thermal and environmental qualification of spacecraft components. As mentioned earlier, a pressure below 1.3×10^{-3} Pa is required to replicate space-like conditions on Earth, and to do so, one must understand the behavior of gases at low pressures and the interactions between residual molecules and system surfaces. This section outlines the classification of vacuum levels, the nature of gas flow regimes, and the principal outgassing phenomena that influence system design and performance.

Vacuum levels are defined based on the pressure inside a sealed vessel and correspond to different molecular behaviors. Table 2.1 summarizes the typical vacuum ranges, compiled based on *ISO* 3529-1 and common engineering literature (International Organization for Standardization, 2011).

Table 2.1 Typical pressure ranges and vacuum levels, compiled from *ISO* 3529-1 and general vacuum literature (International Organization for Standardization, 2011).

Range	Pressure
Rough vacuum	$10^0 ... 10^3$ mbar
Fine/medium vacuum	$10^3 ... 10^0$ mbar
High vacuum	$10^{-7} ... 10^{-3}$ mbar
Ultra-high vacuum (UHV)	$< 10^{-7}$ mbar
Extreme high vacuum (XHV)	$< 10^{-10} or < 10^{-12}$ mbar

The transition between different flow behaviors in a vacuum system is described by the Knudsen number (Kn), a dimensionless ratio defined as:

$$\text{Kn} = \frac{\lambda}{L} \tag{2.6}$$

where λ is the mean free path of gas molecules and L is a characteristic physical dimension of the system (e.g., chamber diameter or pipe length).

Depending on the value of Kn, three distinct flow regimes can be identified:

- **Viscous Flow** (Kn < 0.01): Gas molecules interact primarily with each other; convection and viscous forces dominate.
- **Transition (Knudsen) Flow** ($0.01 <$ Kn < 0.5): A mix of molecular and viscous behavior.
- **Molecular Flow** (Kn > 0.5): Gas molecules interact mostly with chamber walls; convection is no longer relevant.

In high and ultra-high vacuum environments, molecular flow conditions dominate. Under such conditions, the concept of viscosity breaks down, and gas movement becomes random and wall-collision driven (Jousten, 2018). Consequently, traditional conductive or convective heat transport is minimized, and thermal radiation becomes the primary mechanism of energy exchange (Holkeboer et al., 1966). This extremely low pressure also has an effect on the materials and results in outgassing.

Outgassing refers to the release of gas molecules from materials exposed to vacuum. It is a key limiting factor in achieving low pressures and maintaining clean vacuum environments. Four principal mechanisms contribute to outgassing:

- **Desorption**: Release of previously adsorbed molecules from material surfaces.
- **Diffusion**: Migration of gas from within the material bulk to its surface.
- **Permeation**: Ingress of external gas through seals and materials, followed by diffusion and desorption into the chamber.
- **Vaporization**: Phase change of volatile substances at low pressures.

Figure 2.1 depicts the four mechanisims of outgassing just discussed. Outgassing behavior depends on surface condition, material composition, and system temperature. For this reason, vacuum systems are often subjected to *bake-out* procedures, where the internal surfaces are heated prior to testing to accelerate the release of trapped gases and reduce contamination during operation (O'Hanlon, 2003; Jousten, 2018).

Though complex and time-dependent, understanding these mechanisms is vital for test planning and for achieving stable, reproducible low-pressure environments in thermal vacuum facilities.

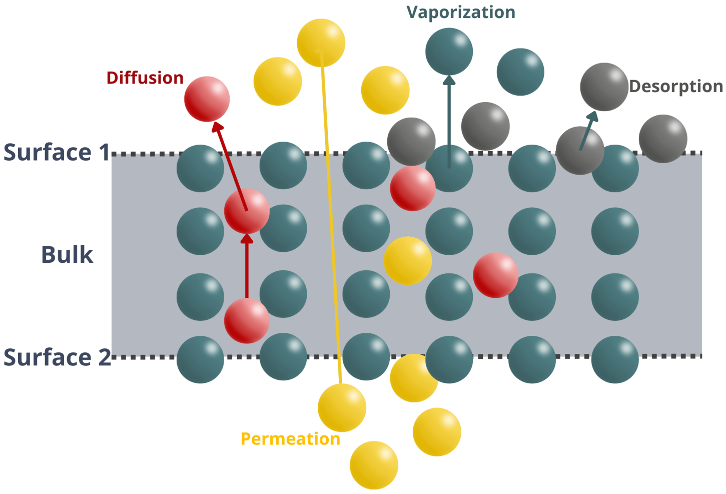

Figure 2.1 Four principal outgassing mechanisms: desorption, diffusion, permeation, and vaporization (Acedera, 2024).

2.3 Thermal Vacuum Chambers and Thermal Shrouds

TVACs are specialized test facilities designed to replicate the vacuum and thermal conditions of outer space. Used extensively in spacecraft qualification campaigns, they evaluate the thermal response, reliability, and survivability of components under representative space conditions. A typical *TVAC* setup consists of three major subsystems: a vacuum generation unit (pressure vessel to maintain low pressure), a thermal conditioning system (to induce controlled heating and cooling), and a mechanically robust pressure enclosure with internal fixtures such as thermal shrouds (to regulate radiative heat exchange).

Vacuum generation is typically achieved using a staged approach. A roughing pump, often a rotary vane or scroll pump, is first used to bring the chamber pressure down from atmospheric to the medium vacuum range. Thereafter, high-vacuum or ultra-high vacuum levels are obtained using turbomolecular or cryogenic pumps (Umrath, 2016; O'Hanlon, 2003). For sensitive space qualification campaigns, cryopumps are often preferred for their oil-free operation and superior cleanliness. Naturally, these are not the only pump types that can be used, Gilmore (2002a) provides a full review on vacuum generation methods.

Thermal conditioning is achieved through active and passive control systems. Cooling is most commonly performed using liquid nitrogen (LN_2), which is circulated through internal cold walls or thermal shrouds. Heating is implemented via electrical resistance heaters, infrared lamps, or embedded heater plates. In high-fidelity test environments, these systems are calibrated to replicate orbital temperature cycles, including eclipse transitions and solar loading (Gilmore, 2002a).

Chamber structure must be capable of withstanding atmospheric pressure while under internal vacuum, which demands high mechanical strength and dimensional stability. Materials such as steel, stainless steel and aluminum alloys are typically employed due to their favorable vacuum compatibility, low outgassing, and thermal stability.

Advanced *TVACs* may also include solar simulators, where Xenon arc lamps configured to reproduce the spectral distribution and irradiance of solar radiation, though these are irrelevant to this project since the focus is on cooling applications. Gilmore (2002b)'s second volume on Cryogenics from the Spacecraft Thermal Control Handbook provides a much more comprehensive understanding of the topic. Holkeboer et al. (1966); however, highlighted the current limitations of conventional heaters / coolers in this context and demonstrated the need for spectrally realistic radiation sources.

As previously mentioned, thermal shrouds are internal radiative enclosures that surround the test article within a vacuum chamber. They provide a defined thermal boundary condition, enabling both steady-state and transient thermal testing under space-like radiative environments. Most shrouds adopt a cylindrical or quasi-cubic geometry to ensure high view factors between their interior surfaces and the test specimen. This improves radiative coupling and temperature uniformity. Shrouds are typically modular to allow access to the test article and to facilitate assembly within the chamber (Haefer, 1972). Shrouds can be operated in either cooling or heating mode. In cooling mode, LN_2 is typically circulated through brazed or welded tubing attached to the shroud panels. In heating mode, either gaseous nitrogen (GN_2) is used or the shroud is equipped with resistive heating elements (Amlinger and Bosma, 1986). Temperature ranges typically extend from $-150\,^{\circ}$C to $+150\,^{\circ}$C, depending on the test requirements.

The inner surfaces of the shroud are usually coated with high-emissivity black paints (e.g., Aeroglaze Z306), achieving emissivity values $\varepsilon > 0.9$. This enhances the uniformity of radiative heat exchange. In contrast, outer surfaces are often left polished or coated with low-emissivity finishes to reduce heat loss, once again, depending on the application and test requirements (Brinkmann, 1984).

Common construction materials include aluminum (notably 6000-series alloys), copper, and stainless steel. Aluminum is preferred for its excellent thermal conductivity and low density, though long-term use has revealed susceptibility to fatigue cracking under thermal cycling. This has led to the adoption of stainless steel in large-scale simulators, such as the *ESA (European Space Agency)* Large Space Simulator (Edwards, 1992; Amlinger and Bosma, 1986). Figure 2.2 shows this chamber, the sun simulator can also be seen active. Fluid channels are typically implemented using extruded profiles, brazed tubing, or machined grooves to ensure even temperature distribution across the panel surfaces. A more comprehensive study on potential materials that can be used is discussed later on in this documentation.

In conclusion, thermal shrouds support multiple test objectives such as Thermal balance testing, i.e. determination of steady-state temperature distributions under known external and internal heat loads.

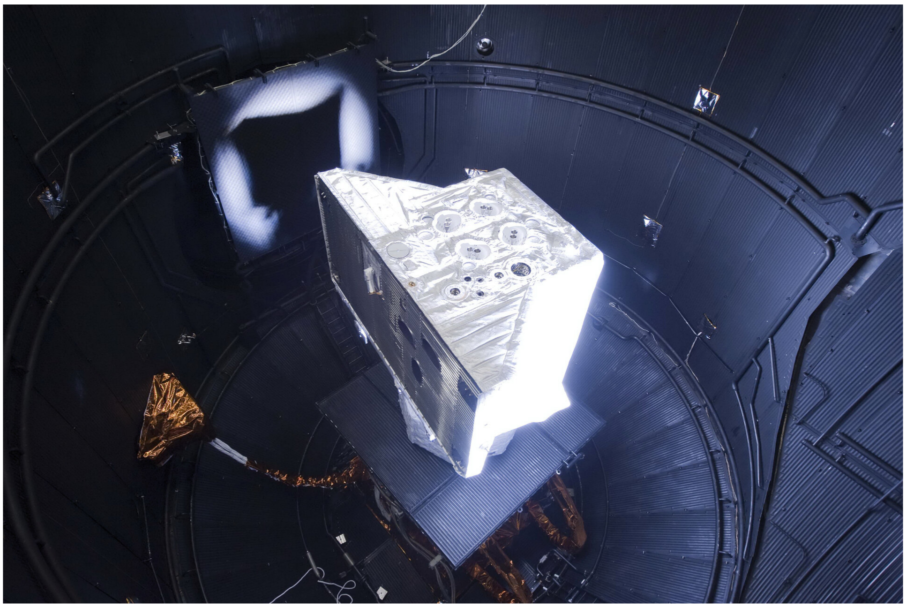

Figure 2.2 The European Space Agency's Large Space Simulator at ESTEC, illustrating sun simulation and LN2-cooled floor [Image credit: European Space Agency (2024).

Thermal shrouds also support thermal cycling, which is the repeated heating and cooling to assess material fatigue and system resilience, as well as Outgassing-sensitive tests which provide clean radiative surfaces and minimizing contamination risk through material preconditioning. Shrouds do so working in parallel with a hot/cold plate. Various types of cold plates exist and a select few are to be discussed in section 5. Overall, this short literature review divulged that thermal plates and shrouds are a fundamental enabling element of thermal vacuum testing. Their design directly impacts the fidelity, repeatability, and efficiency of spacecraft thermal qualification campaigns. Readers interested in further details on thermal vacuum testing are referred to Gilmore (2002a)'s Spacecraft Thermal Control Handbook and Jousten (2018)'s Handbook of Vacuum Technology.

3 LISA Chamber

The *LISA* vacuum chamber, named after the "Lightweight Inter-Satellite Link Antenna" (*LISA*) project previously conducted at the Technical University of Munich (*TUM*), is a cylindrical steel structure designed for thermal-vacuum testing of satellite components and other planetary exploration equipment. The chamber is now located at the Professorship of *LPE* on the premises of the *TUM* in Ottobrunn, Germany. The *TVAC* is capable of achieving high vacuum levels down to 10^{-5} mbar and used to support temperature ranges from $-75\,^{\circ}\mathrm{C}$ to $+100\,^{\circ}\mathrm{C}$ through its integrated thermal shroud system.

3.1 Chamber Geometry

The *LISA* vacuum chamber is a cylindrical high-vacuum chamber with an internal diameter of 650 mm, external diameter of 660 mm and an internal length of 1020 mm. On the inside, there are six attachment points, three on each side, that are used for mounting telescopic rails which carry the cold plate. These attachment points are spaced 442.5 mm apart. The chamber also has 16 attachment points that can be used to mount a shroud. This is further discussed in section 6.4. Figures 3.1a and 3.1b show drawings of the chamber along with relevant dimensions.

The chamber is also equipped with a variety of ISO-KF flanges. A breakdown of their sizes, quantities and locations are shown in Table 3.1. These flanges are not directly relevant to the project, except for that they need to be accessed from inside and so are only briefly summarized here.

Table 3.1 KF flange sizes, quantities, and locations on the LISA chamber.

KF Size	Diameter [mm]	Quantity	Location(s)
KF16	16	1	Top of the chamber towards the back door
KF40	40	9	3 on front door, 4 on back door, 2 on chamber body
KF63	70	1	Front door
KF100	100	1	Back door
KF150	150	9	3 on left side, 3 on right side, 3 on top of the chamber cylinder
KF250	250	2	1 on front door, 1 on back door

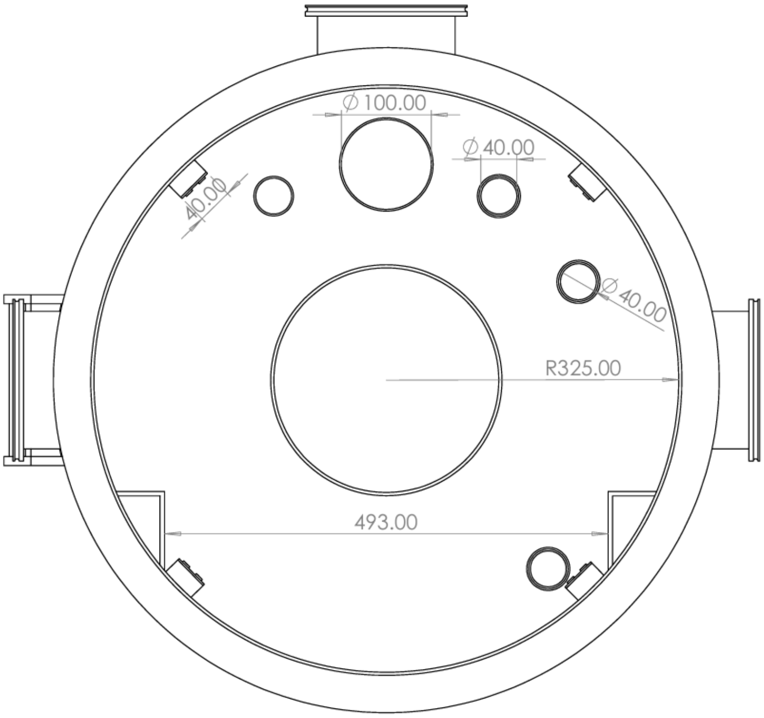

(a) The chamber as seen from the front.

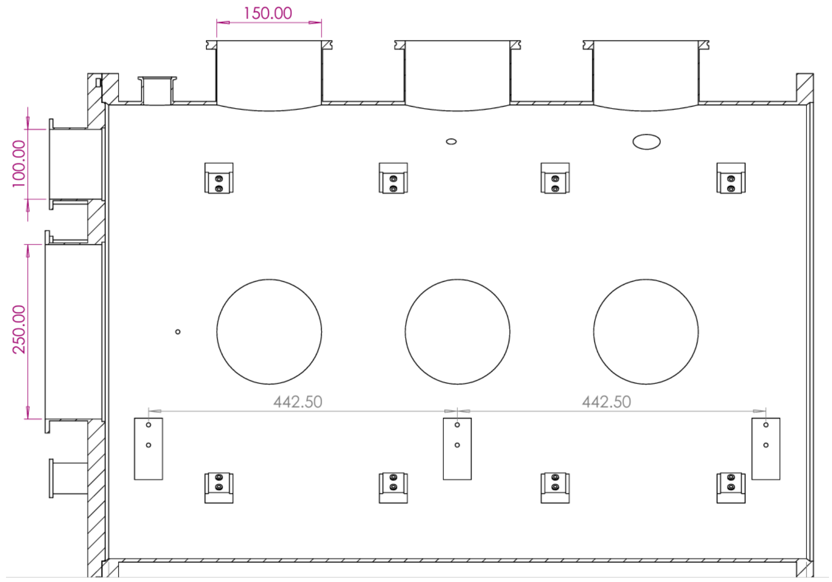

(b) Section view of the chamber depicting spacing between telescopic rails' mounting points.

Figure 3.1 Dimensional Drawings of the Lisa vacuum chamber.

3.2 Previous Cold Plate & Shroud System

The *LISA* chamber included a complex integrated cold plate and thermal shroud system that supported temperature ranges from $-75\,^{\circ}\mathrm{C}$ to $+100\,^{\circ}\mathrm{C}$. The system had an $\sim$ 880x420 mm cold plate with surface-mounted cooling/heating tubes. Both the plate and the tubes are made from aluminum. Figure 3.2 shows the geometry of the cold plate tubes as well as dimensional drawing of the plate.

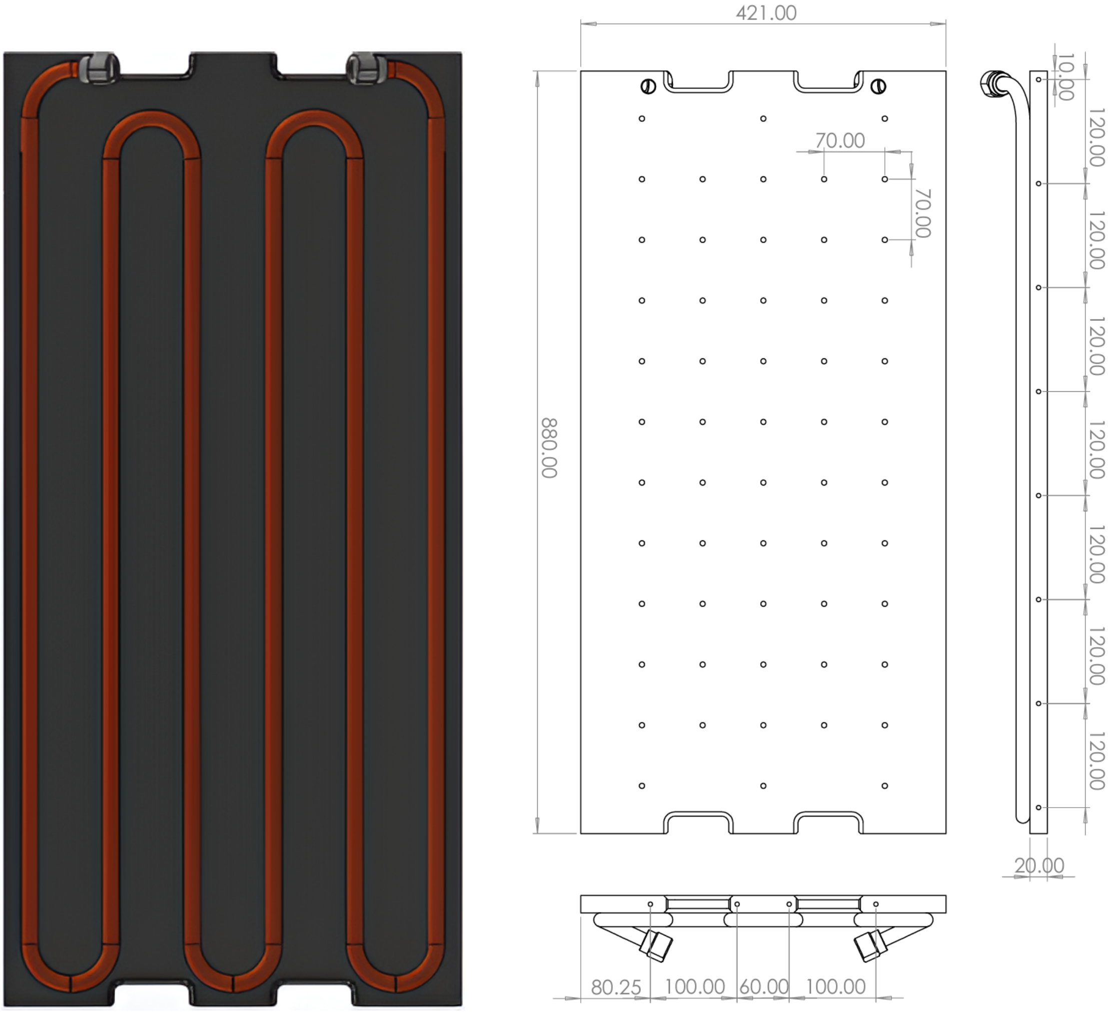

(a) The geometry of the tubes attached to the cold plate as seen from below.

(b) Dimensional drawing of the cold plate depicting various hole spacing throughout the plate.

Figure 3.2 Geometry and layout of the previous aluminum cold plate installed in the LISA chamber.

The plate also featured a number of holes for integration with the telescopic rails and mounting equipment. On the side of the cold plate are 8 holes, 120 mm apart, that are used to connect to the rails. These are shown in the figure above and are further discussed later on in this documentation. The plate also has a number of threaded holes at the topside that can be used for various applications. These holes are separated 70 mm apart on both the x- and y-axis.

The cold plate also has a pair of side platforms onto which are 90° elbows to mount the door side shrouds. These panels also have surface-mounted cooling/heating tubes. At the top of the shroud are openings for flexible pipes that can be used for experiments. Figure 3.3 shows this assembly.

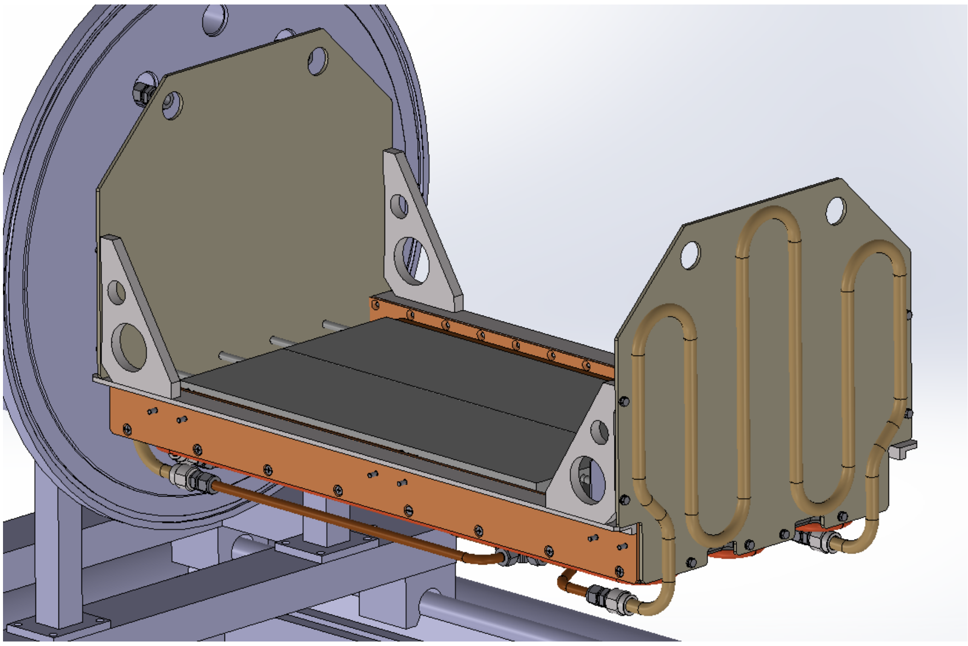

Figure 3.3 Door-side shroud with cooling elbows and surface-mounted tubing, part of the original system.

The side platforms are also there partially to support the relatively heavy tube-cooled upper shroud. The upper shroud follows the same principle as the door shroud. All these panels are 5 mm thick and have tubes welded to its surface. The upper shroud had only two small openings to provide visual access from one of the side windows and a top window. Figure 3.4 depicts the full assembly of the previous system.

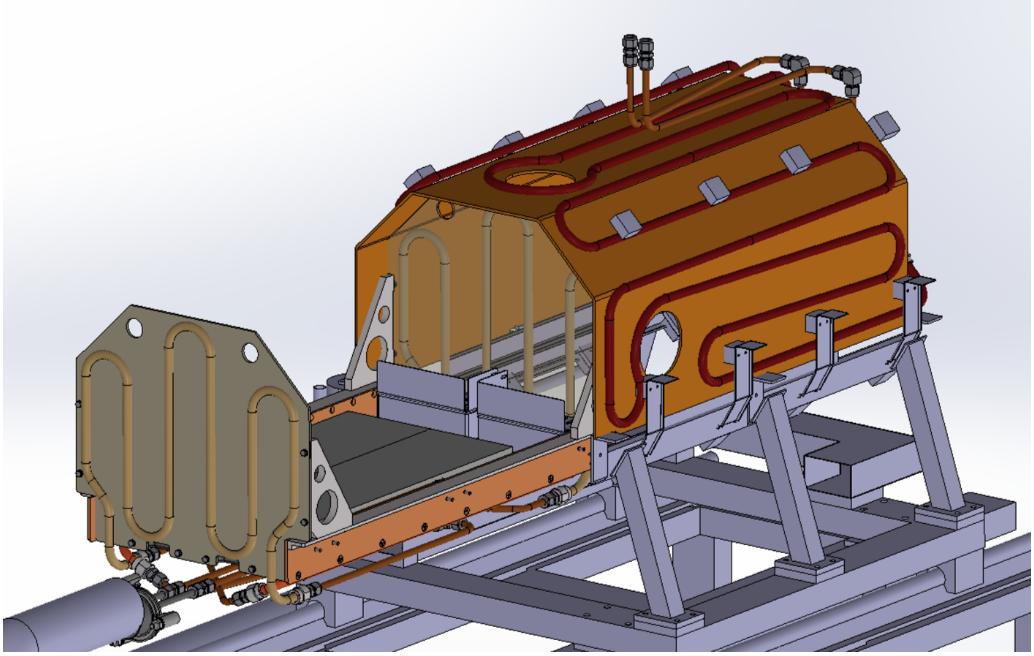

Figure 3.4 Full assembly of the original cold plate and thermal shroud system.

Additionally, the previous system had a complete layer of *MLI (Multi-Layer Insulation)* on the inside of the chamber, covering all cylindrical walls as well as the doors of the chamber. Figure 3.5 shows what the *MLI* looked like when it was first installed. This has naturally, degraded over the years and now has regolith and coolant trapped within it due experimentation and leakage.

Figure 3.5 Multi-layer insulation inside the *LISA* chamber when first applied.

The previous setup also had a a box from which thermocouples were allowed to be connected throughout an expermintal setup. There were also connected to parts of the shroud and cold plate to measure their temperatures. This box is depicted below in Figure 3.6.

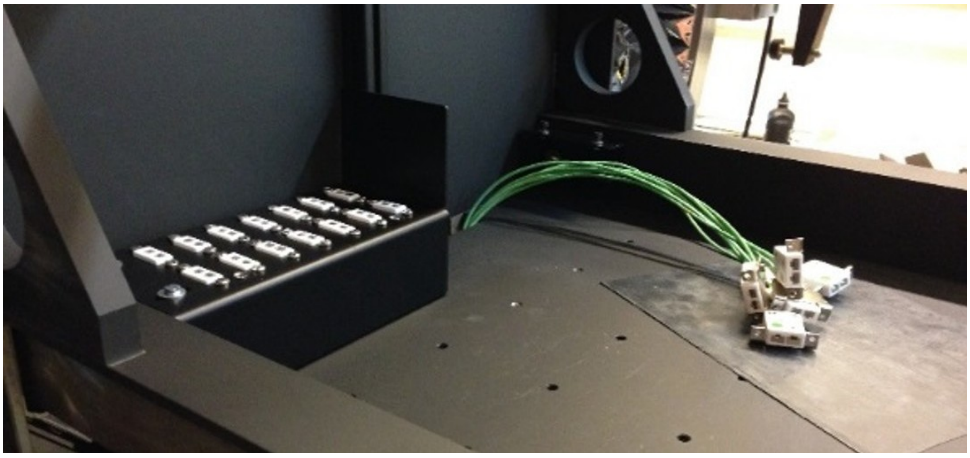

Figure 3.6 Thermocouple connection box used in earlier experiments with the cold plate and shroud.

4 Objective and Scope

4.1 Scope & Outline

The purpose of this documentation is to evaluate the existing cold plate and shroud system installed in the *LISA* thermal-vacuum chamber, and to design and analyze a revised solution that improves thermal performance, experimental flexibility, and spatial efficiency. The study focuses on assessing the thermal viability of the previous setup, identifying key shortcomings, and proposing new concepts that better meet the requirements of current and future use cases.

The existing system showed a number of limitations. The thermal shroud was oversized and occupied a significant portion of the experimental volume, which constrained usable space and interfered with mounting hardware. Additionally, the previous shroud included surface-mounted coolant tubes, and a large number of fittings connecting to them. This made the design bulky, and potentially, contributed to fluid leakage. Multi-layer insulation installed in the chamber has degraded over time and become contaminated with regolith and coolant from previous experiments, further diminishing the system's integrity (see Figure B.3 in the appendix).

This project therefore investigates alternative configurations for the thermal shroud and reassesses the viability of the existing cold plate. All design proposals are intended to support future experiments in a high vacuum, dusty environment, with particular emphasis on minimizing radiative losses, accommodating mechanical constraints, and allowing modular upgrades.

4.2 Future Case Studies

A key future experiment to be conducted within the *LISA* chamber is the *RPS (Rover Permittivity Sensor)* project. This sensor, developed for integration into the Rashid-3 rover, is designed to measure the dielectric permittivity of the lunar regolith through a wheel-mounted electrode system. These permittivity measurements provide insights into water content in the subsurface, offering crucial data for resource mapping and planetary science.

To replicate lunar conditions, the wheel must roll over a regolith bed inside the chamber. The wheel has a diameter of 200 mm, requiring a travel distance of approximately 630 mm for one full revolution. This necessitates a substantial, unobstructed experimental area above the cold plate. Moreover, supporting structures, such as a gantry to move the rover or sensors, may be installed inside the chamber. This imposes additional constraints on the design of the thermal shroud, which must minimize its footprint while providing effective thermal shielding.

Multiple chamber ports are also required for cameras, sensors, and instrumentation. These ports must remain unblocked by any shroud configuration to ensure proper data acquisition and visual monitoring during experiments. Figure 4.1 shows a *CAD* of the *RPS*.

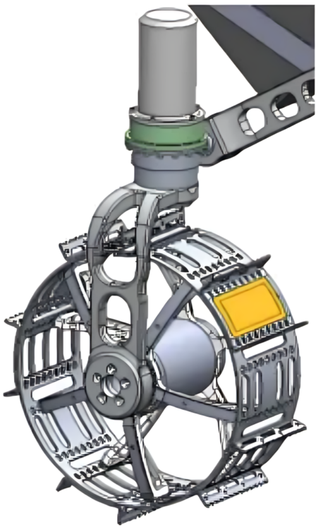

Figure 4.1 CAD of the rover permittivity sensor wheel when attached to the Rashid-3 rover.

4.3 System Requirements

The following system-level requirements were derived from the project goals and future experimental needs:

- The cold plate shall support a removable regolith box for sample loading and unloading.
- The cold plate shall be mechanically compatible with the existing telescopic rail system.
- The cold plate and shroud shall remain thermally decoupled to prevent parasitic heat conduction.
- The thermal shroud shall fit within the remaining internal volume of the chamber while maximizing available space for the gantry and experimental equipment.
- The system shall provide adequate clearance for a 200 mm diameter rover wheel to traverse at least 630 mm across a regolith surface.
- The thermal shroud shall not obstruct key optical or diagnostic access ports required for future experiments.
- The final design should allow for easy removal and reconfiguration to support different experimental setups.

These requirements serve as the foundation for evaluating design alternatives and determining the most suitable solution given the constraints of the *LISA* chamber and upcoming test campaigns.

5 Cold Plate

The cold plate is the heart of the system's conductive heat sink. It plays a central role in absorbing and transporting thermal energy away from the regolith and other components used in experiments. This chapter outlines the conceptualization, design choices, and integration strategies employed in the analysis of the previous and new system. The chapter covers coolant selection, coolant supply systems, plate type comparisons, internal channel geometries, mechanical interfaces, and concludes with a set of key takeaways and recommendations.

5.1 Coolant Selection

Initially, the analysis of the cold plate assumed *LN2 (Liquid Nitrogen)* to be the working fluid, mainly due to its widespread use in thermal vacuum applications and its extremely low boiling point of -196 ℃. The assumption was that for roughly a day's worth of testing, 8 hours, 200 L of liquid nitrogen would be consumed. With this in mind, some rough thermal estimate calculations were conducted for the rover permittivity sensor experiment.

Given the masses and materials of the current cold plate and chamber, in addition to an estimated mass of regolith that is to be used during the rover permittivity system experiment, initial analysis of the 200 L over 8 hour assumption was conducted. While an idealized calculation might indicate that the cooling demands could be met with a relatively modest amount of *LN2*, this is quickly dismissed once more realistic inefficiencies and additional thermal loads are added to the equation. The cold plate would have a 10 cm thick regolith bed on top of it, which is not easy to cool down to the desired temperature. Once the bed is added to the calculation, achieving a temperature change of 100 ℃ or 140 ℃ would actually require a prohibitively large amount of *LN2*. This cooling requirement non-conformity was one of the primary reasons for considering alternative coolants. A system with a closed-loop circulation and improved manageability, might be better suited to the experimental conditions.

Eventually, *HFE-7100* was selected as the coolant fluid. Hydrofluoroethers (HFEs) are a class of organic solvents originally developed as a replacement for ozone-depleting chemicals. *HFE-7100* serves as a 1:1 replacement for 3M™ Novec™ 7100 (3M, 2022). It offers a boiling point of approximately 61 ℃, which, while significantly higher than *LN2*, still enables effective heat absorption and transfer for the scope of the experiments to be conducted. The fluid is non-conductive, chemically stable, and is compatible with a wide range of materials, including metals and polymers used in the chamber and cooling system (Puretecs GmbH, 2023). More importantly, *HFE-7100*'s liquid state under operating conditions allows for closed-loop circulation, which is required for the extreme cooling demand of the thick regolith bed.

5.2 Coolant Supply System

The circulation of the *HFE-7100* coolant is handled by the Huber Unistat 1015w (Figure 5.1). This is a high-performance, water-cooled thermal control unit designed for precise and stable temperature regulation. It offers a 4 kW heating capacity and a cooling performance of 2.5 kW at temperatures from 100℃ down to -40℃, depending on the thermal fluid used. That; however, is not the lowest temperature achievable, the Unistat offers a working temperature range of -120℃ to +100℃. The extremely low temperature, while desirable, is challenging to maintain with a static shroud. As for flow properties, the internal pump, made from stainless steel and magnetically coupled, delivers up to 44 liters per minute and a maximum pressure of 1.5 bar (Huber Kältemaschinenbau AG, 2023). This ensures reliable coolant flow through the cold plate even under varying thermal loads.

Figure 5.1 Huber Unistat 1015w thermal control system used for closed-loop circulation of *HFE-7100* coolant (Huber Kältemaschinenbau AG, 2023).

Control is handled via the Pilot ONE interface, a touchscreen-based system. Precise temperature adjustments are offered with a resolution of 0.01 K. The unit supports Ethernet, USB, and RS232 connections, along with standard safety features like overtemperature protection and fluid level monitoring (Huber Kältemaschinenbau AG, 2023). Overall, the Unistat 1015w coupled with the *HFE-7100* coolant provide the reliability and performance necessary for repeated thermal experiments within the dirty vacuum chamber.

5.3 Plate Types

The first step when considering a new cold plate was to evaluate the available options. Three cold plate types were investigated during the design phase: microchannel plates, embedded tube plates, and vacuum brazed plates.

Figure 5.2 An example of a Microchannel cold plate with fine internal pathways.

Microchannel plates feature tiny channels etched or machined into the plate. This offers high surface area-to-volume ratios and hence, excellent heat transfer characteristics. These plates are ideal for applications with high heat flux. Given that the vacuum chamber would now feature a static shroud as opposed to a fluid-cooled one, the additional losses incurred need to be recouped through maximizing cooling performance. That being said, the downside to this type of cold plate is that not only are the complex internal structures prone to clogging, especially in environments where particulate contamination is possible, which is a known risk in dirty vacuum chamber setups, but also that the manufacturing process of these plates is quite complex and therefore, expensive. Off-the-shelf options of this plate type do not come in the size required for this chamber and a custom made plate of the required scale would simply be too expensive (Khan and Fartaj, 2011). Figure 5.2 shows what such a plate looks like.

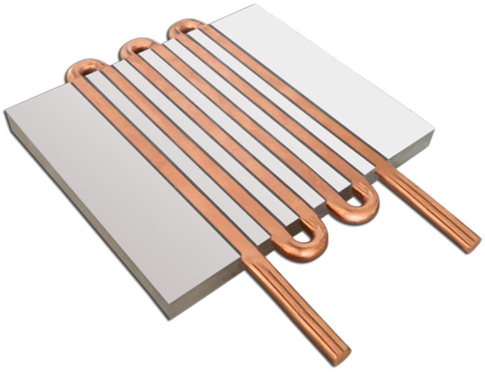

Figure 5.3 An example of an Embedded tube cold plate.

Embedded tube plates consist of a metal base, usually copper or aluminum, with tubes embedded within (see Figure 5.3), hence the name. This evaluated type is the most similar to the old plate discussed in section 3.2. The coolant flowing through the tubes absorbs and dissipates heat. The design offers robust thermal performance and simplicity in manufacturing, making it cost-effective. However, since there exists a contact interface between the tubes and the metal base, thermal contact resistance is higher and can lead to localized inefficiencies (Mersen, 2024).

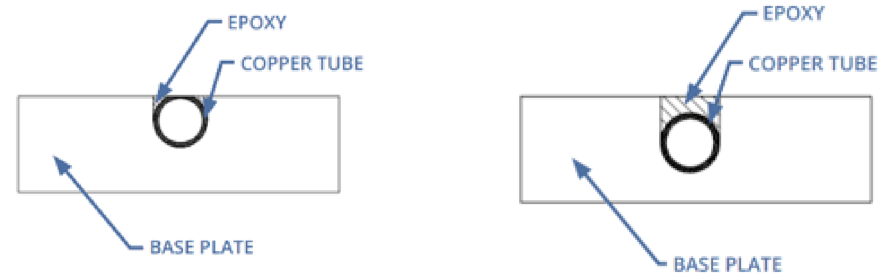

(a) Near-surface embedded tubes with an epoxy layer

(b) Deeply embedded tubes with an epoxy layer

Figure 5.4 Section views of embedded tube cold plates.

However, more crucially, when considering that this plate would operate in vacuum conditions, there exists risks of outgassing and delamination . As seen in Figure 5.4, there is a layer of epoxy covering the tubes, and that has high potential for outgassing. Furthermore, this outgassing risk can be coupled with delamination risk. Thermal cycling and vacuum stresses can lead the separation of layers and outgassing further fuels this as trapped volatile compounds within the epoxy can vaporize in a vacuum. If these vapors cannot easily escape, they can build pressure at the bonding interface. Contrarily, if these vapors manage to escape, they can leave behind voids or bubbles within the epoxy layer, which also weakens the bond and creates stress concentration points that can initiate delamination (Boyd Corporation, 2025).

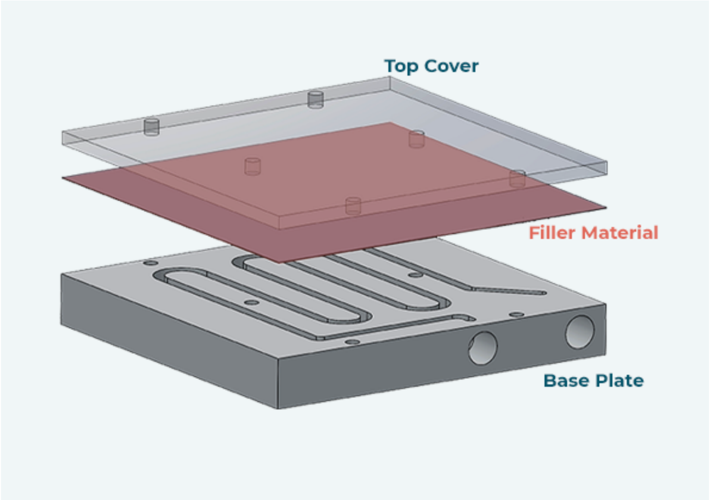

Figure 5.5 An example of a vacuum brazed cold plate concept.

The final plate type considered is the vacuum brazed cold plate. These plates are made through the joining of two or more metal plates and melting a filler metal material (see Figure 5.5). This filler material has a lower melting point and is typically a brazing alloy (Mersen, 2024). A variation of this plate also exists in which instead of using a filler material, friction stir welding is applied along the sides to join the two plate pieces together, these are sometimes referred to as *FSW (Friction Stir Welded)* cold plates. For both variations, the internal geometries can be customized for uniform cooling, and the sealed design hint that this type of plate is the most suitable for vacuum conditions. That being said, off-the-shelf options for this plate were found with a maximum length of $\sim$ 600 mm, which might be acceptable except that the width range is between 250-300 mm, and so, a single plate is too small and two plates have a combined width that exceeds the chamber geometry. Therefore, further consideration of this plate type would require a custom-designed plate.

Given all considerations, vacuum brazed plates were selected as the basis for a potential new cold plate and a few channel geometries were proposed for evaluation. The next step was to assess their internal fluid pathways.

5.4 Cooling Channel Geometry

To further evaluate the potential of vacuum brazed or *FSW* cold plates as a replacement to the current setup, the first step was to generate a few channel geometries. Figure 5.6 shows two proposed channel geometries along with the old cold plate for reference.

To evaluate the hydraulic performance of two cold plate geometries, the total pressure loss in each configuration is estimated. Since both designs use the same coolant (*HFE-7100*), the same pipe diameter of 15 mm, and are connected to the same pump delivering a constant flow rate of 44 L/min, a few simplifications can be made. Considering that the fluid velocity is relatively high, a Reynolds number check confirms fully turbulent flow. The general pressure losses equation is divided into frictional and minor losses:

$$\Delta P_{\text{total}} = \Delta P_{\text{friction}} + \Delta P_{\text{minor}} \tag{5.1}$$

$$\Delta P_{\text{total}} = f \cdot \frac{L}{D} \cdot \frac{\rho v^2}{2} + \sum K \cdot \frac{\rho v^2}{2} \tag{5.2}$$

Where:

- f is the Darcy friction factor
- L is the total flow length
- D is the pipe diameter
- v is the average flow velocity
- ρ is the fluid density
- K are loss coefficients from bends

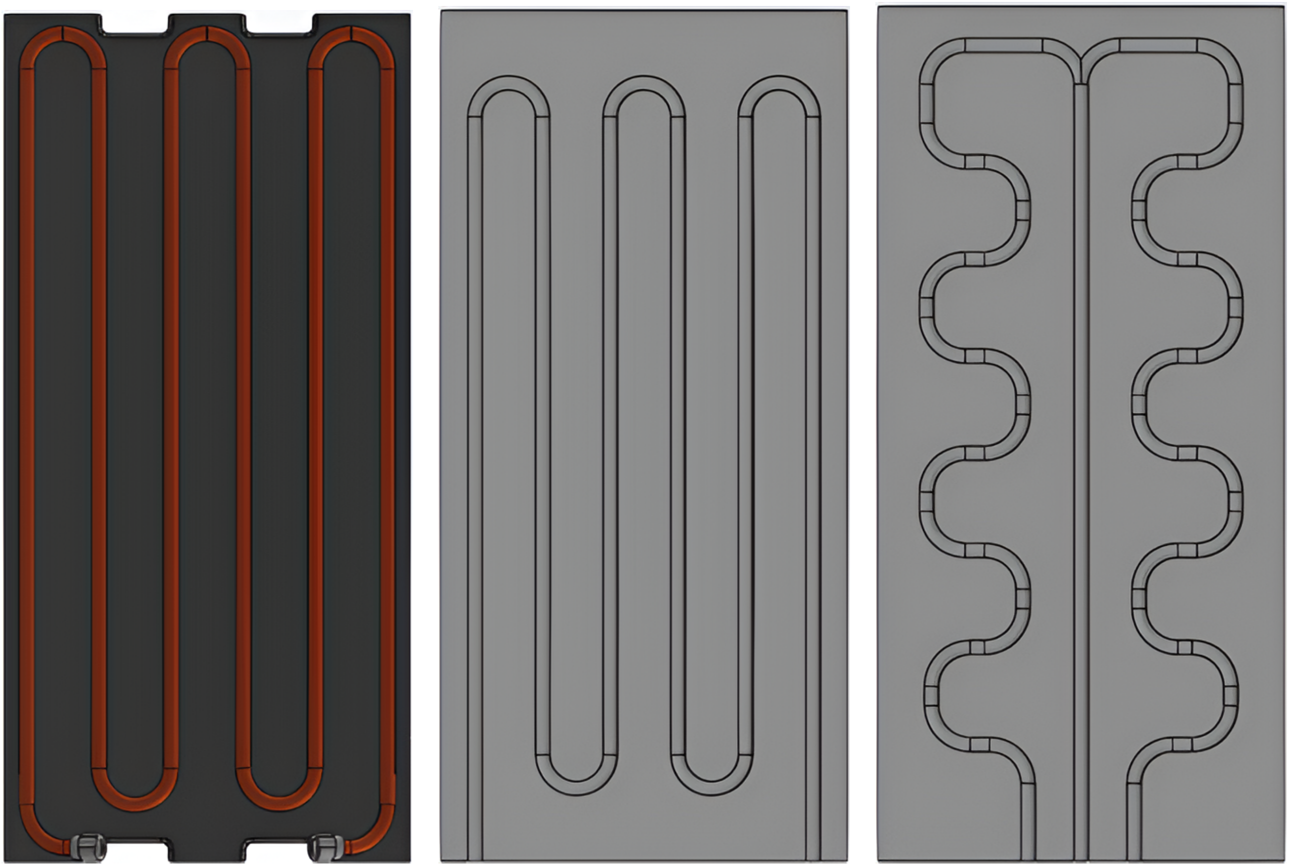

(a) Old plate single-path channel geometry.

(b) Proposed single-path channel design (Plate 1).

(c) Proposed dual-leg channel design with central inlet and split flow (Plate 2).

Figure 5.6 Comparison of old and proposed cooling channel geometries within cold plates.

The Darcy friction factor, f and the loss coefficients from bends, K are empirical parameters used to estimate pressure losses due to wall friction and localized flow disturbances such as bends or fittings. The dynamic viscosity of the coolant, *HFE-7100* was taken as $\mu = 0.00061\,\text{Pa}\cdot\text{s}$, based on data provided in the 3M product datasheet (3M, 2022) at room temperature (approximately 25℃). Before assuming values for the Darcy friction factor and loss coefficients from bends, a few more fluid properties were derived first:

- Density: $\rho = 1520\,\text{kg/m}^3$
- Dynamic viscosity: $\mu = 0.00061\,\text{Pa}\cdot\text{s}$
- Diameter: $D = 0.015\,\text{m}$
- Volumetric flow rate: $Q = 44\,\text{L/min} = 7.33 \times 10^{-4}\,\text{m}^3/\text{s}$

Cross-sectional area:

$$A = \frac{\pi D^2}{4} = \frac{\pi (0.015)^2}{4} \approx 1.77 \times 10^{-4}\,\text{m}^2 \tag{5.3}$$

Flow velocity:

$$v = \frac{Q}{A} = \frac{7.33 \times 10^{-4}}{1.77 \times 10^{-4}} \approx 4.15\,\text{m/s} \tag{5.4}$$

$$\text{Re} = \frac{\rho v D}{\mu} = \frac{1600 \cdot 4.15 \cdot 0.015}{0.00061} \approx 164{,}000 \tag{5.5}$$

Fully turbulent flow is confirmed, so we assume a friction factor:

$$f = 0.03$$

Here, a value of $f = 0.03$ was assumed, which is typical for fully turbulent flow in smooth metallic pipes when specific surface roughness data is unavailable (Shah and Sekulic, 2003). Given that both plates are assumed to be from the same manufacturer, this value offers a reasonable basis for comparison. The loss coefficients depend on geometry; for example, a 180° bend with a bend radius of four times the pipe diameter has a typical K value of 0.4, while standard 90° bends commonly have $K = 0.25$. These values are sourced from experimental data presented in references such as Crane Technical Paper 410 (Crane Co., 2018).

Next, the pressure losses are calculated separately for both plates. The proposed first plate's pipe geometry has 4180 mm of 'straight' segments and a total of 5 180 degree turns. Given this, the calculation is conducted as follows:

Plate 1:

- Straight segments: $L = 4.18\,\text{m}$
- 5 × 180° bends with $r/D = 4$, $K = 0.4$ (Crane Co., 2018)
- Turn length: $L = 0.55\,\text{m}$
- Total length: $L_{\text{total}} = 4.73\,\text{m}$

The dynamic pressure is:

$$\frac{\rho v^2}{2} = \frac{1600 \cdot (4.15)^2}{2} \approx 13\,778\,\text{Pa} \tag{5.6}$$

Pressure loss for Plate 1, through substituting in Equations 5.1 and 5.2:

$$\Delta P_{\text{friction}} \approx 130\,\text{kPa} \tag{5.7}$$

and the minor loss:

$$\Delta P_{\text{minor}} \approx 27.6\,\text{kPa} \tag{5.8}$$

Thus,

$$\Delta P_{\text{plate 1}} \approx 157.6\,\text{kPa} \tag{5.9}$$

The pressure losses experienced in the first plate were calculated to be roughly 157.6 kPa. When comparing this to the maximum output pressure of 1.5 bar, given the assumed plate properties, the losses are greater than the supplied pressure. The second plate's proposed pipe geometry is slightly different in that it has a single inlet but two outputs. This plate's pressure losses can now be evaluated through these steps:

Plate 2:

- Common inlet: $0.8\,\text{m}$ of pipe
- Each leg: $1.465\,\text{m}$ of pipe
- Total leg length: $L = 0.8 + 1.465 = 2.265\,\text{m}$
- Flow per leg: $Q = 22\,\text{L/min} = 3.67 \times 10^{-4}\,\text{m}^3/\text{s}$
- Velocity in each leg:

$$v_{\text{leg}} = \frac{3.67 \times 10^{-4}}{1.77 \times 10^{-4}} \approx 2.08\,\text{m/s} \tag{5.10}$$

16 × 90° bends per leg, $K = 0.25$ (Crane Co., 2018) an so the common inlet, the friction loss is:

$$\Delta P_{\text{inlet}} = 0.03 \cdot \frac{0.8}{0.015} \cdot 13\,778 \approx 22\,\text{kPa} \tag{5.11}$$

For each leg, the dynamic pressure is:

$$\frac{\rho v_{\text{leg}}^2}{2} = \frac{1600 \cdot (2.08)^2}{2} \approx 3\,428\,\text{Pa} \tag{5.12}$$

The friction loss per leg is:

$$\Delta P_{\text{friction,2}} = 0.03 \cdot \frac{2.265}{0.015} \cdot 3\,428 \approx 15.7\,\text{kPa} \tag{5.13}$$

The minor loss per leg is:

$$\Delta P_{\text{minor,2}} = 16 \cdot 0.25 \cdot 3\,428 \approx 13.7\,\text{kPa} \tag{5.14}$$

Thus, the total drop per leg is:

$$\Delta P_{\text{leg}} \approx 29.4\,\text{kPa} \tag{5.15}$$

Adding the inlet loss, the total pressure drop for Plate 2 is:

$$\Delta P_{\text{plate 2}} \approx 22\,\text{kPa} + 29.4\,\text{kPa} \approx 51.4\,\text{kPa} \tag{5.16}$$

Although Plate 2 features more bends (Sixteen 90 degree bends), its design includes a common inlet that splits the flow into two parallel legs. This reduces the velocity in each branch, thereby significantly lowering the friction and minor losses. As a result, Plate 2 is better suited for a pump with a maximum pressure of 1.5 bar, while Plate 1 is closer to this limit. It also offers the advantage that the cooling starts from the middle of the plate outwards, as opposed to from one side to the other.

These designs were then sent to manufacturers for a cost estimate. One contact agreed to produce the plate, though from copper instead of aluminium and with a maximum size of 450x450 mm. As discussed in section 3.2, the old cold plate is 880x420 mm, meaning that two new plates would be required for the vacuum chamber. Each plate would cost roughly 5000 Euros and the system would have twice the number of fittings, which increases risk of leakage.

5.5 Mounting & Interfaces

The cold plate is mounted to the rest of the vacuum chamber using a pair of telescopic rails. While the telescopic rails themselves are beyond the scope of this project, they serve as the primary conduction pathway between the cold plate and the rest of the chamber. Therefore, the interface between the cold plate and the rails, as well as between the rails and the chamber walls, is briefly discussed.

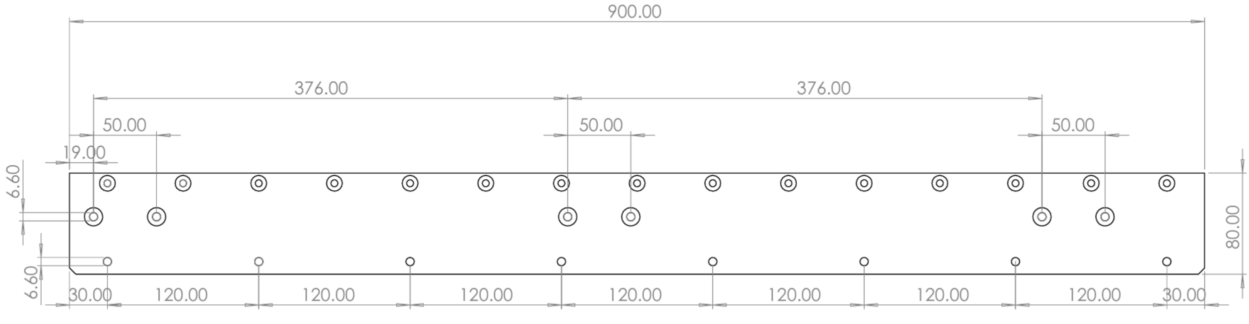

Figure 5.7 Mounting adapter plate interface between the cold plate and telescopic rails, showing hole spacing and support platform connections.

The previous cold plate featured eight equally spaced 5 mm holes for mounting. The spacing between the holes is 120 mm. The telescopic rail however, featured three pairs of 6.6 mm openings that are suitable for M6 bolts. Each pair of openings are spaced 50 mm apart (Rollon GmbH, 2024). This means that an adapter is required between the cold plate and the rails. This adapter already exists and its dimensions are summarized in Figure 5.7.

The fifteen upper holes are there for a supporting platform onto which the door shroud mounts. The conduction heat transfer decoupling between the cold plate and the door shroud will be further discussed in section 6.6. This adapter plate is 5 mm thick and is potentially made from steel, though uncertain due to the presence of a sprayed-on paint layer. In any case, the thermal insulation is achieved using *PTFE (Polytetrafluoroethylene)* sheets located between the adapter mounting holes and the telescopic rails. These sheets are 1 mm thick and 3-4 layers are used to provide the necessary insulation.

Figure 5.8 shows the location of the previous fluid feed-through relative to the cold plate. While this fluid feed-through would be replaced with a smaller DN40 version with VCR fittings and requires a DN 63-40 CF reducer, meaning that it would be located slightly more to the left compared to Figure 5.8, it still poses a challenge to connect the cold plate to the coolant supply through it. The use of VCR fittings compared to traditional fittings is desired due to VCR fitting's superior leak tightness. A flexible tube would have too high of a minimum bend radius than what is required to connect the cold plate to the feed-through. Alternatively, a CNC bent tube can be used here. While this would be a viable choice, there exists a simpler and vastly cheaper option where the cold plate assembly is simply rotated the other way around so that the inlet and outlet for the cold plate is on the other side of the chamber. Then, a longer and already available flexible

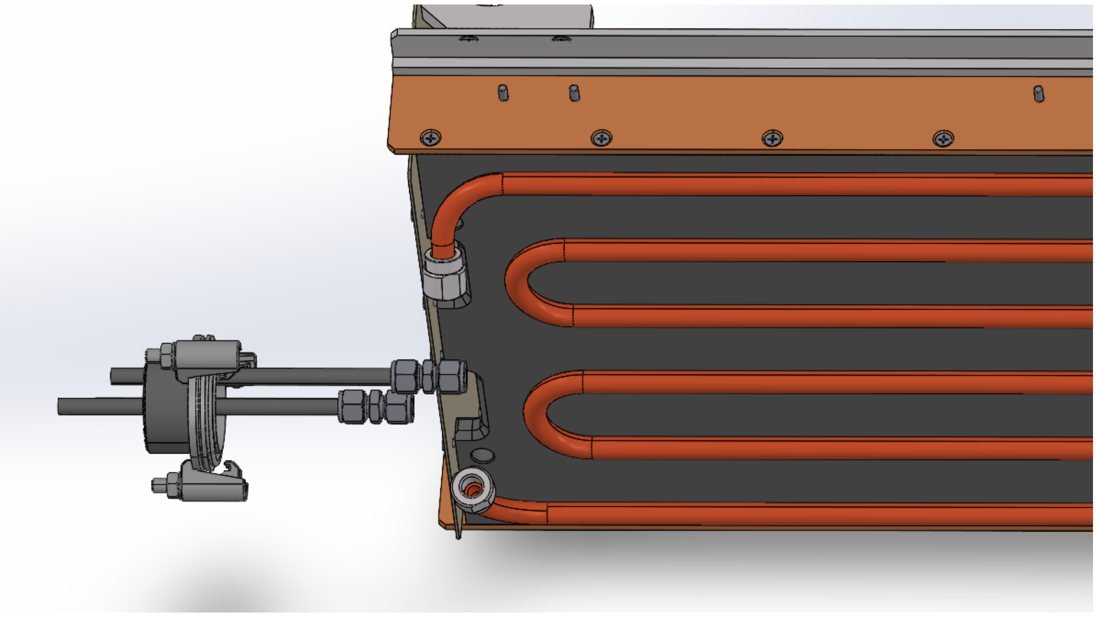

Figure 5.8 Previous fluid feed-through location relative to cold plate.

tube would be used. The longer distance between the cold plate inlet and outlet and the fluid feed-through implies that even if the flexible tube option was to be replaced with a solid pipe sometime in the future, accurately aligning the pipe to the fluid feed-through is significantly easier.

5.6 Summary & Recommendations

The chapter aimed to analyse and evaluate alternative cold plate solutions to fulfill the low temperature requirement derived from future experiments. At first liquid Nitrogen was assumed as the working fluid but then replaced with *HFE-7100* as the coolant. This change practically had no influence on the rest of the analysis. The coolant would be circulated using the Huber Unistat 1015w system. After evaluating alternative cold plate types, the vacuum brazed or *FSW* cold plates were selected as favorites to replace the old system. The Unistat's properties were used as boundary conditions to analyse the pressure losses across two proposed channel geometries within the cold plates.

The pressure losses calculations point towards the second proposed channel geometry as the potential replacement candidate to the old plate. However, the estimated cost of this change is ~ 10.000 Euros. At this moment, such a change is out of budget and so the old cold plate must remain the working plate. Nonetheless, the alternative plate remains a viable candidate for future implementation.

With the old plate now remaining as the working plate for the vacuum chamber, the integration of the cold plate is simpler since the adapter and interfaces to the telescopic rails and the rest of the chamber remains the same. However, the design of the shroud system now faces the challenge of additional thermal loses from the lower side of the cold plate.

6 Thermal Shroud

The thermal shroud is the subsystem primarily responsible for radiation shielding between the chamber walls and the experimental volume. Given that the cold plate remains unchanged, the thermal shroud now faces the additional challenge of additional radiative losses from the lower side of the plate. This makes it a challenge to try and maintain as low a temperature as possible within the chamber. This chapter outlines the concept development, material selection, thermal analysis, and the resulting final design of the shroud. Particular attention is given to the trade-offs between multi-layer configurations and the rationale behind the chosen design, including its integration and mounting strategy within the chamber.

6.1 Concept Design

The initial phase of the design process focused on evaluating different shroud configurations with the goal of minimizing radiative heat loads while maintaining accessibility and mechanical compatibility. Three configurations were considered: a single-layer, a double-layer, and a triple-layer shroud. Each layer corresponds to an additional shell of reflective aluminum sheets separated by Teflon spacers. Figure 6.1 depicts the increasing layers of shroud.

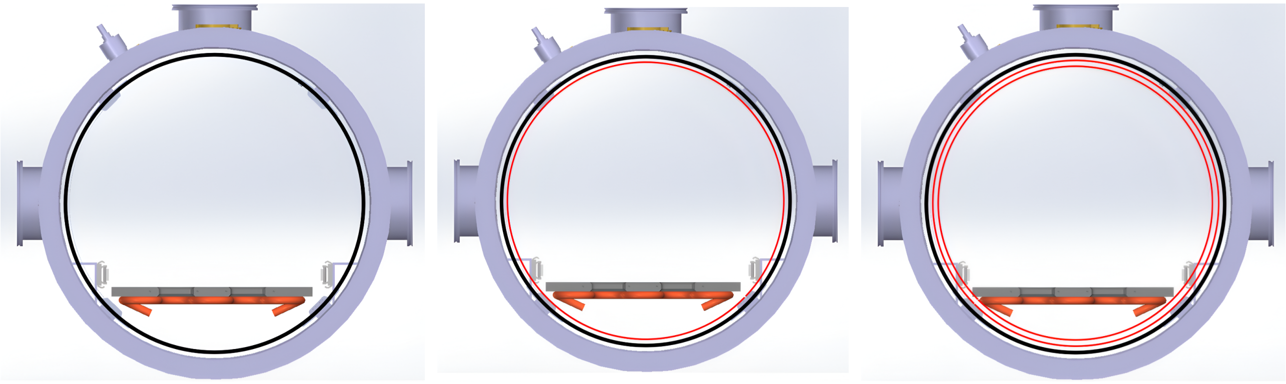

(a) Single shroud layer. **(b)** Double shroud layers. **(c)** Triple shroud layers.

Figure 6.1 Conceptual sketches of thermal shroud multi-panel configurations within the chamber. In black is the first layer, then each additional layer is depicted in red.

The triple configuration, although theoretically would be beneficial in reducing radiative heat transfer, this option was discarded early in the trade-off simply due to interference with the telescopic rail system.

The triple-layer shroud option can be seen in Figure 6.1c. Moreover, the triple configuration would take up too much space within the chamber; therefore limiting the available space for the required gantry system and other supporting equipment.

When comparing the single layer configuration to its double layer counterpart, a trade-off between available space and thermal performance is considered and evaluated. The double layer configuration depicted in Figure 6.1b takes up additional space compared to a single layer, but the question of whether or not sacrificing this space is worth it or is necessary is yet to be answered. To do so, first the material for the shroud as well as the insulators need to be selected.

6.2 Material Selection

The material selection process for the thermal shroud was guided by a set of functional requirements. These are: high thermal reflectivity to minimize radiative heat exchange, mechanical stability under vacuum conditions, ease of fabrication, compatibility with vacuum environments (i.e. low outgassing), and cost-efficiency.

First a comparison between aluminum, copper and stainless steel is considered. Copper, while offering the highest thermal conductivity, was eliminated due to its higher weight, cost, and reduced reflectivity compared to aluminum. Stainless steel, while it provides mechanical strength and structural stability, it has low thermal conductivity and higher emissivity, making it unsuitable for this application. Therefore, Aluminum, with its high infrared reflectivity, low density, ease of fabrication, and widespread availability at a reasonable cost emerged as the preferred choice.

Next, several aluminum alloy series were considered. Those are the 1000, 2000, 5000 and 6000 series alloys. Table D.2 in the appendix includes a full comparison between these alloy series, including their references. Table 6.1 below shows a summary of that comparison conducted that includes the properties that are more relevant to this application.

Table 6.1 Summary of selected properties for aluminum alloy series (Gilmore, 2002a; Davis, 1993).

Alloy Series	**6000**	**5000**	**2000**	**1000**
Thermal Conductivity [W/m·K]	166	121–152	120	235
Thermal Diffusivity [mm^2/s]	$\sim$63	$\sim$55	$\sim$50	$\sim$90
Formability	Moderate	Easy	Difficult	Easy
Availability	High	High	Moderate	High
Cost	Low	Low	High	Low

Given that the shroud would be thin and the absence of significant mechanical loads, high strength was not a design requirement. The 1000 series alloy instantly stood out for its high reflectivity, low emissivity if polished, and excellent formability. These are all characteristics critical to this application. The exact thickness of the shroud sheets was initially set as 0.5-1 mm. The final choice depends on availability. Ultimately, as seen in section 6.5, the sheets were determined to be 0.75 mm thick. This should provide sufficient rigidity while minimizing thermal mass for the intended purpose of the shroud.

Finally, the material used for thermal insulation was to be evaluated. The three choices considered were Teflon (*PTFE*), Vespel and *PEEK (Polyether Ether Ketone)*. The criteria used for evaluation were thermal performance (conductivity and diffusivity), manufacturability, and availability/cost, though the last criteria is the main driving factor here. Table D.1 in the appendix shows some relevant properties for the three materials. Between the three choices, Teflon emerged as the preferred choice. It has low thermal conductivity and is widely available. It is also, by far, the cheapest option. Now that materials have been assigned to the shroud and insulators, the evaluation of the number of shroud layers can proceed.

6.3 Simulation & Analysis

To evaluate whether a single or double layer of shroud is necessary, steady-state thermal simulations were conducted in *COMSOL (COMSOL Multiphysics)*. These simulations, while crude, serve as a basis for comparison between the configurations. These simulations modeled the chamber environment under vacuum, with a fixed boundary condition (temperature) set to the tubes of the cold plate. The modules used were heat transfer in solids as well as surface-to-surface radiation. The material for the shroud was assigned as aluminum with properties acquired from section 6.2 above. Additionally, the chamber wall (steel) and the cold plate (aluminum) materials were assigned. The fixed temperature within the tubes was set a 153 K (-120 ℃), which is the lowest temperature the Unistat and *HFE-7100* can provide.

Other properties, also derived from earlier chapters, were initially used to for a transient multi-physics simulation that included fluid flow, heat transfer in solids and fluids, and surface-to-surface radiation. However, these simulations did not produce sensible results and since a numerical analysis is not the main focus of this project, these simulations were discarded. This is further discussed and reflected upon in section 7.2. Before proceeding with the steady-state simulations of the various configurations, a baseline is established with a simulation that included no shroud at all.

Figure 6.2 shows the resulting contours from the steady-state thermal simulation of the cold plate within the chamber. This resulted in an average chamber temperature of 278 K. The temperature is averaged because there existed a thermal gradient between the upper and lower sides of the chamber. This is due to the exposed pipes underneath the cold plate. Figure 6.3 below depicts this temperature gradient. The

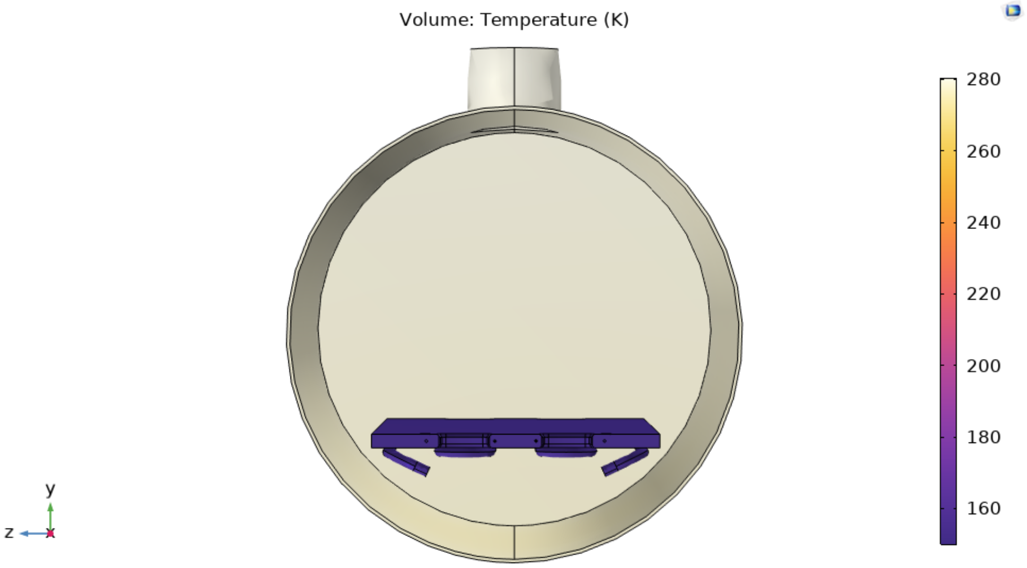

Figure 6.2 Temperature contours of a steady-state simulation involving only the chamber and cold plate.

lowermost point of the chamber had a temperature of 276 K while the uppermost point had a temperature of 281 K. Whether or not this temperature gradient persists in the shrouded configuration will later be evaluated.

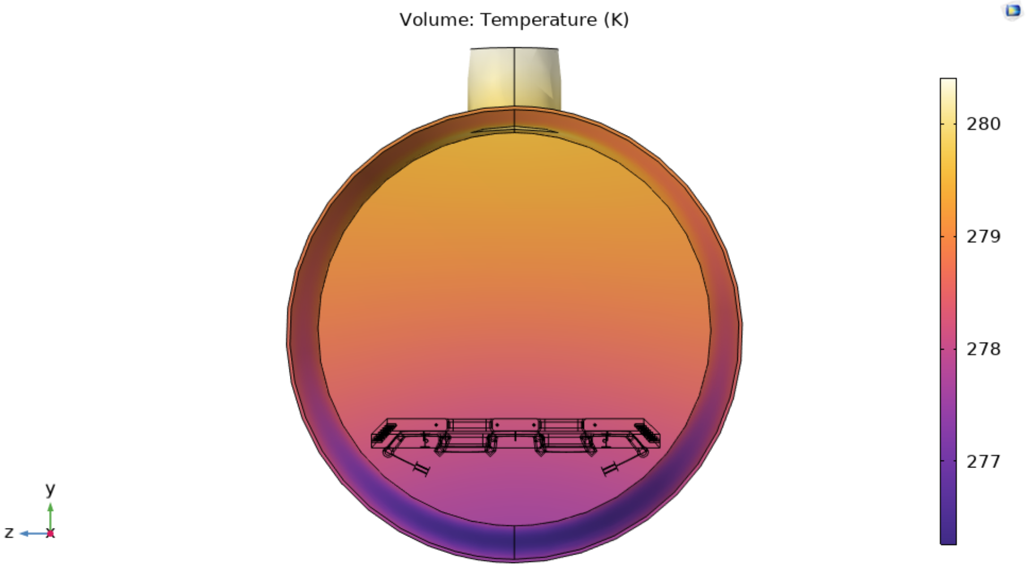

Figure 6.3 Re-scaled temperature contours of the steady-state simulation involving only the chamber and cold plate.

Figures 6.4 and 6.5 show the temperature contours for the single and double shroud configuration, respectively. While both maintained an outer chamber wall temperature of roughly 284 K, the temperatures for the shroud(s) were different. The single configuration had an average shroud temperature of 268 K. This, relative to the baseline simulation, shows a ΔT of roughly 10 K. The double shroud configuration had an average temperature for the first layer as 271 K and 260 K for the second layer. For the sake of comparison, the temperature of the layer closest to the cold plate is always used. This means that the $\sim$

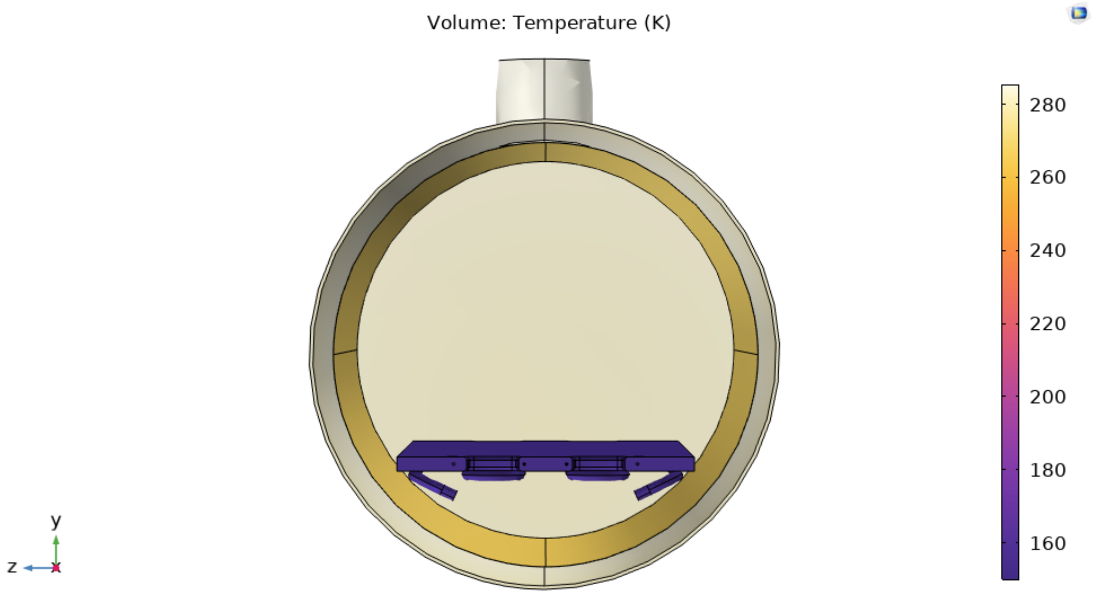

Figure 6.4 Temperature contours of a steady-state simulation involving the chamber, cold plate and a single layer of shroud.

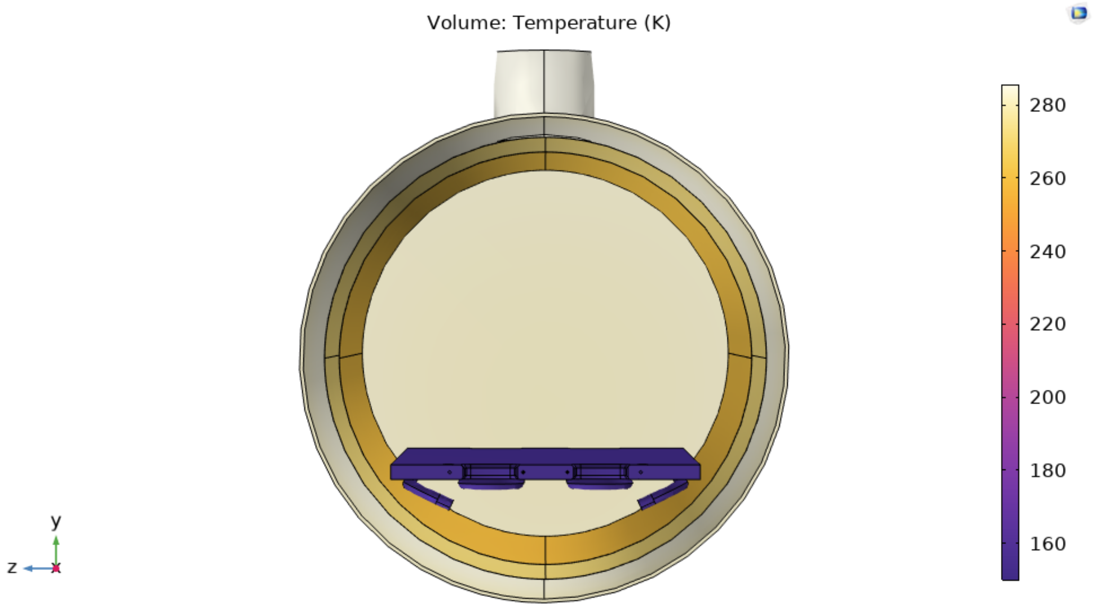

Figure 6.5 Temperature contours of a steady-state simulation involving the chamber, cold plate and a double layer of shroud.

260 K of the second layer points towards an additional ΔT improvement of roughly 8 K. Therefore, the use of a second layer retained 80% of the improvement seen between a no shroud configuration and a single-layer shroud configuration and so the use of a double-layer shroud at the expense of available space might be worth it. However, these temperatures are presented as averages since the temperature gradient across the shroud layer persisted. This is depicted in Figures A.1 and A.2 of the appendix. The effect of the temperature gradient decreased as the number of layers increased. In any case, a third configuration

was premised on the idea that since there existed a gradient between the upper and lower parts of the shroud, a configuration in which a single layer is used then a second layer is applied only to the lower part of the chamber might offer an acceptable compromise.

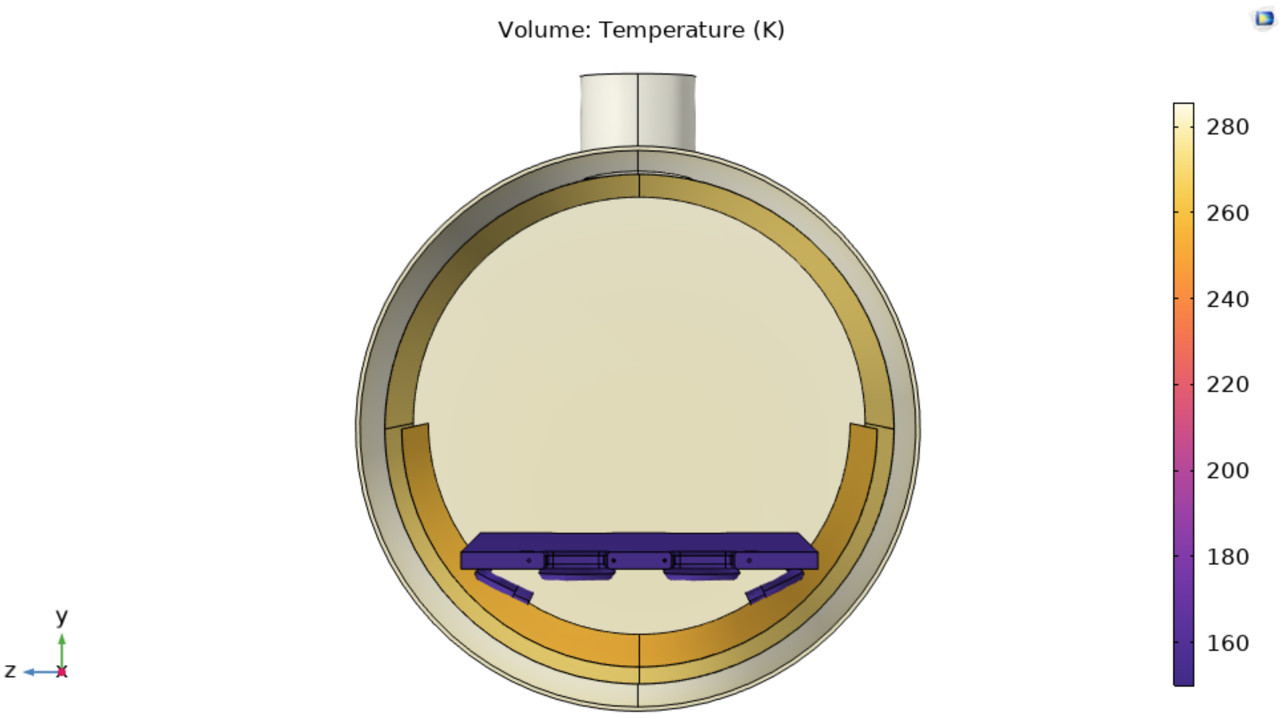

Figure 6.6 Temperature contours of a steady-state simulation involving the chamber, cold plate, and 1.5 layers of shroud.

Figure 6.6 depicts the contours generated for the steady-state thermal simulation of the additional proposed configuration. A single-layer shroud is applied to the entire chamber and a second layer is only applied to the lower half. This resulted in average temperatures for the first layer and second layer of 270 K and 258 K, respectively. When comparing this to the first and second layer temperatures of the full double-layer configuration (271 K and 260 K respectively), the difference between these configurations is only 1-2 K. Therefore, this configuration seems to provide almost the same thermal performance, while providing additional space at the top half of the chamber for the gantry system and other supporting equipment.

The next step is to develop a final concept that can be implemented and integrated into the chamber. Figure 6.7 shows the final concept as seen from the front of the chamber. Implementing this concept as a single sheet that surrounds the entire chamber is impractical. Additionally, the half shroud depicted earlier reaches up until the half of the chamber. Practically, the second layer cannot be implemented that high since there are no attachment points at the middle of the chamber. To better reach a final design, the mounting points and interfaces between the chamber and the shroud need to be discussed first.

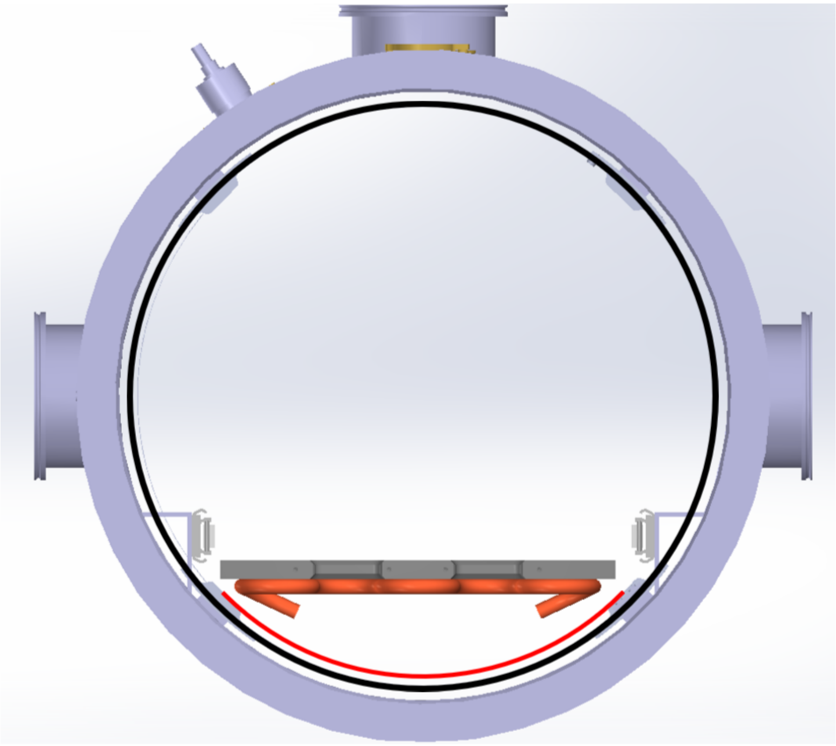

Figure 6.7 The final concept of the thermal shroud considering attachment points' location.

6.4 Mounting & Interfaces

The chamber features a total of 16 attachment blocks available to mount the shroud. These are configured along 4 equally-separated rows. Each row has 4 attachment blocks. Figures B.4 and B.2 in the appendix show these blocks within the chamber. Since there exists 4 rows that are each 90° apart, the idea was to have modular sheets or panels bent into concentric arcs along the chamber wall that can be interchanged and easily replaceable. Unfortunately, each 4-pair circular instance of these blocks is not equally spaced to the following 4-pair circular instance. This is better depicted in Figure 6.8. This means that the same sheet cannot be used along all three 'columns' of the chamber. That being said, the same panel can be interchangeably used along the same 'column', i.e. a panel mounted towards the top of the chamber can be used at the bottom or on one of the sides.

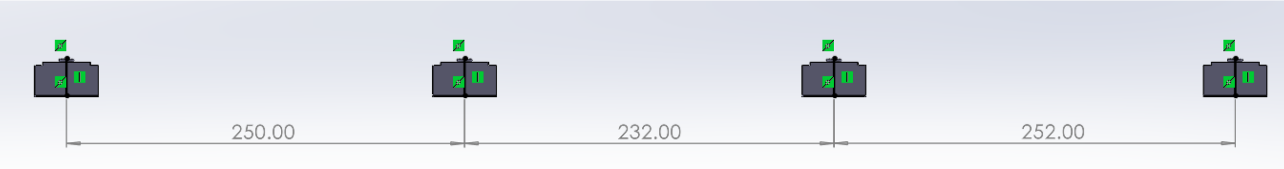

Figure 6.8 Uneven spacing of internal attachment blocks inside the chamber.

A closer look on a single attachment block shows a pair of M5 holes that are 20 mm apart. Figure 6.9 shows a cross section of one of the blocks. While these holes are roughly 7-8 mm deep, the threaded region is only 2-3 mm, depicted in red. This is a concern for when assembling the shroud.

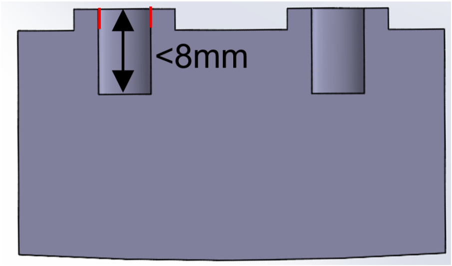

Figure 6.9 Cross-section of a mounting block showing shallow M5 thread depth.

Even with just a single shroud layer of shroud, the space available for mounting the gantry system is barely usable. Therefore, an evaluation of where the first layer of the shroud is to be mounted was conducted. Figure 6.10a shows the initial position at which the first layer is mounted (in red) and the proposed shifting of that position further behind the attachment point (in green). Figure 6.10b then compares both options and highlights in grey, the useful space intended to be utilized for the gantry system. The shifting back of the shroud is now necessary and an adapter needs to be designed to mount the shroud further behind the attachment blocks.

Since this adapter would directly interface with the attachment blocks and hence the chamber, ideally it should be made from an insulating material. Given the analysis of potential insulating materials earlier in section 6.2, this adapter is to be made from Teflon. Figure 6.11 shows what the adapter looks like as well as a cross-section depicting how the Teflon blocks fit onto the attachment blocks. Additionally, engineering drawings of this block are available in the appendix.

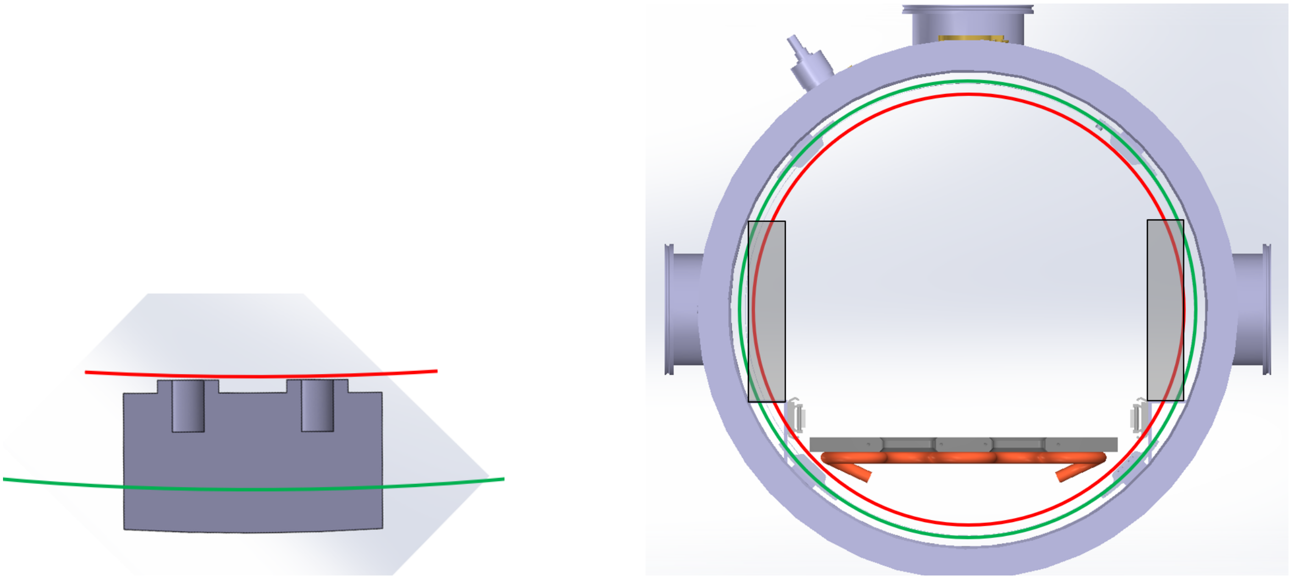

(a) Section view of the attachment point depicting where the proposed start of the first layer is.

(b) Front view of the chamber depicting the generated useful space (shaded).

Figure 6.10 Comparison of first-layer placement position and the generated useful space (shaded region). In red is the initial position, and in green is the suggested change.

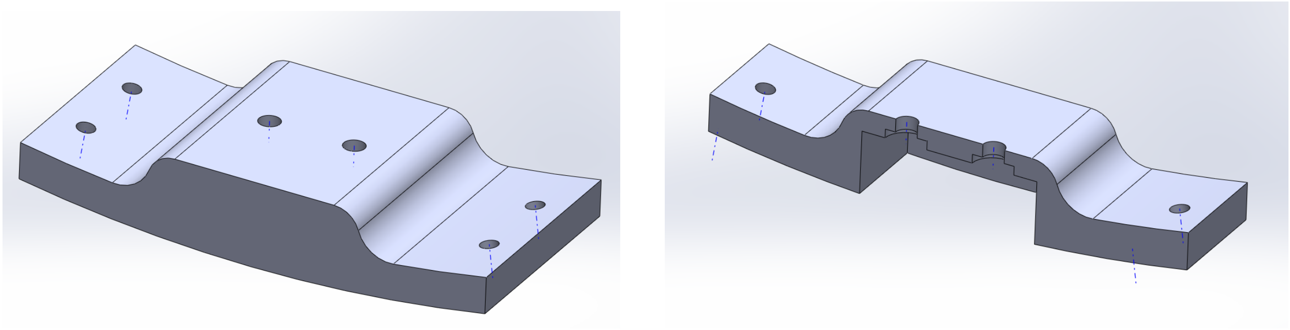

(a) The general shape of the adaptor. Its curvature follows that of the chamber.

(b) Section view of the adapter depicting where the mounting block attaches to.

Figure 6.11 *CAD* of Teflon adapter block.

Next, the shroud is to be mounted to the Teflon blocks. Considering that the distance between the bottom of the Teflon block and the chamber wall is only 10 mm, there is not enough space to rotate a bolt from underneath the Teflon block, and holding a nut underneath the Teflon block is challenging especially considering that some of these assemblies would be located at the middle of the chamber. Additionally, to remove a single sheet layer, the entire bolt assembly would need to be removed. To overcome these challenges, first, an M4 hex head bolt is inserted from beneath the Teflon block and a bolt is inserted from the top to fix the bolt in place. Afterwards, alternating layers of Teflon spacers/washers and aluminum shroud sheets are inserted, depending on the number of layers required. Figure 6.12 depicts what such an assembly would look like for a section with two layers of shroud.

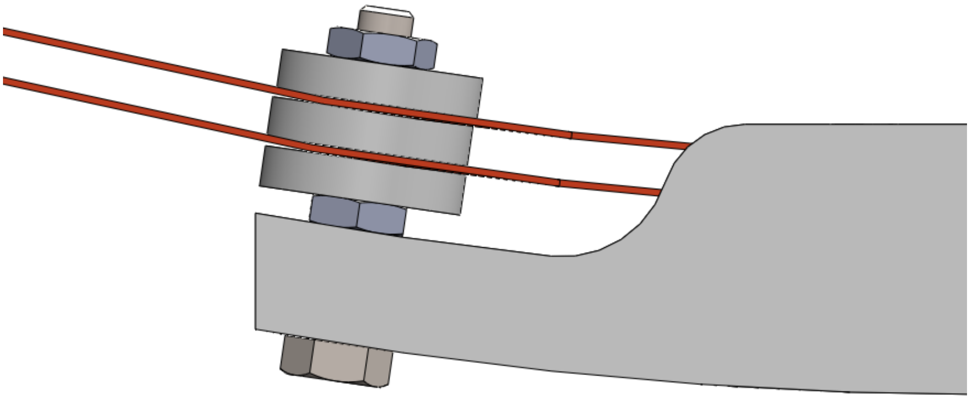

Figure 6.12 Mounting configuration with alternating Teflon spacers and aluminum layers.

6.5 Final Design

As discussed earlier, the idea was to design modular and interchangeable aluminum sheets or panels. However, due to the irregularities and asymmetry in the chamber, several sheet panels need to be design. Nonetheless, they all were derived from and follow the same concept. Figure 6.13 depicts what such a sheet looks like.

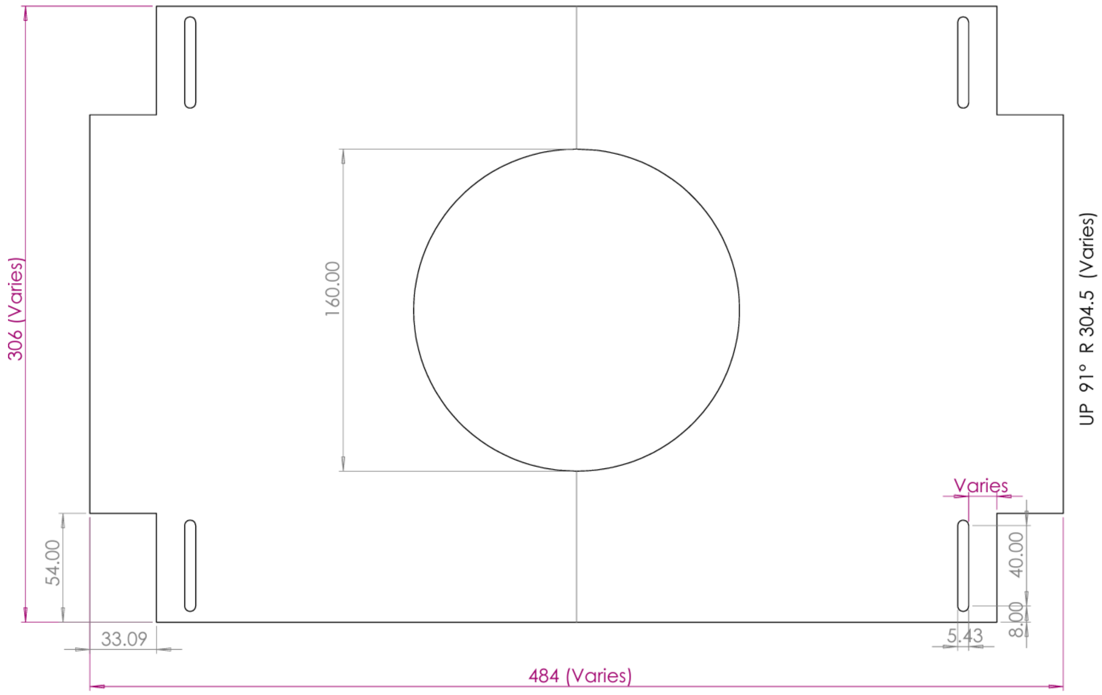

Figure 6.13 Sample dimensional drawing of an aluminum sheet panel.

As seen in Figure 6.13 above, some of the mentioned dimensions varies from one sheet to another. The 306 mm dimension on the far left depends on where along the chamber 'columns' the sheet would be located, i.e. whether the sheet is at the front, middle, or back of the chamber. Recall Figure 6.8 where the spacing between the attachment points varied and so the width of the sheet would vary as well. The 484 mm dimension seen at the bottom of the drawing as well as the R 304.5 radius seen at the far right vary depending on whether the sheet is the first layer or the second layer. Finally, the space between the mounting slot and the edge next to it varied as it is this spacing that was used to align the slots of staggered sheets with each other. This is further discussed at the end of this section.

Initially, the sheets did not feature a 40 mm wide mounting slot, instead, there were a pair of M5 holes at each corner of the sheet. These holes needed to align perfectly with the holes of another layer underneath them (if applicable) and then the teflon block holes as well. Accurately measuring the distance between pairs of holes that are relatively far apart is challenging and the alignment of these holes is critical, especially when considering thermal stresses.

During an initial feasibility study of this design, a quick thermal expansion check calculation was made. Assuming uniform temperature increase ΔT and free expansion:

$$\Delta L = \alpha L \Delta T \tag{6.1}$$

Where,
α is the coefficient of thermal expansion = $23e-6$ /℃ (Davis, 1993)
L is the unsupported vertical span $\approx 0.39m$
ΔT is an arbitrary temperature change = $120K$

$$\therefore \Delta L \approx 1.1mm$$

This means that the plate could expand/contract by $\sim 1.1mm$, potentially misaligning mounting holes and so the design decision of switching to mounting slots naturally accommodates the expansion/contraction. If displacement due to thermal stresses was to occur along the short axis of the sheet, then the sheet would just slide along the slot, and if displacement was to occur along the long axis, then the sheet would simply bend slightly more or less, depending on whether it expands or contracts.

Another concern when dealing with thin sheets is the deflection of a thin sheet under its own weight. For small sheets, this deflection is negligible, but for large thin sheets with longer unsupported lengths, the sheets may deflect or sag. To quickly verify this, the maximum deflection can be calculated assuming the sheet acts as a simply supported thin rectangular plate with four supports:

$$\delta_{\text{max}} \approx \frac{5wL^4}{384EI} \tag{6.2}$$

Where:
w is the weight per unit area and is given by: $\rho g t = 2700 \cdot 9.81 \cdot 0.0005 = 13.24\,\mathrm{N/m^2}$ (uniform load)
L is the unsupported vertical span $\approx 0.39\,\mathrm{m}$
E is the Modulus of Elasticity = $70 \times 10^9\,\mathrm{Pa}$
I is the moment of inertia and is given by: $\frac{t^3}{12} = \frac{(0.0005)^3}{12} = 1.04 \times 10^{-14}\,\mathrm{m}^4$

$$\therefore \delta_{\text{max}} \approx 1.64\,\mathrm{mm}$$

Therefore, while the thermal expansion must be accounted for, the deflection proved to be not of concern, especially when considering that the sheet thickness ended up being 0.75 mm as opposed to the 0.5 mm used in the calculation.

Next, the basic sheet design shown earlier in Figure 6.13 was to be modified to produce variants throughout the chamber. This produced two design variants for each of the front and back end of the chamber, one is with a window opening, and the other is identical but closed. However, the middle layers had 3

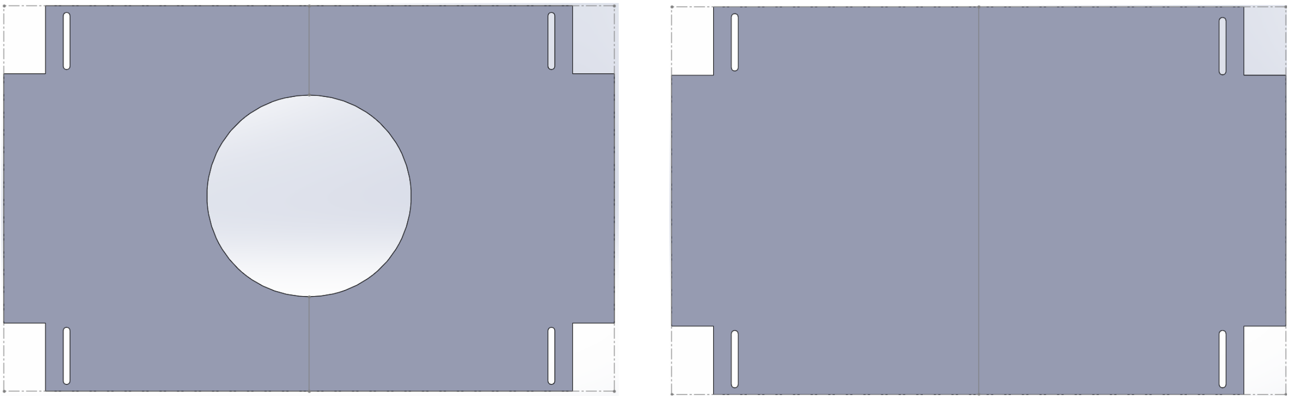

(a) Front-side panel with window. **(b)** Front-side panel without window.

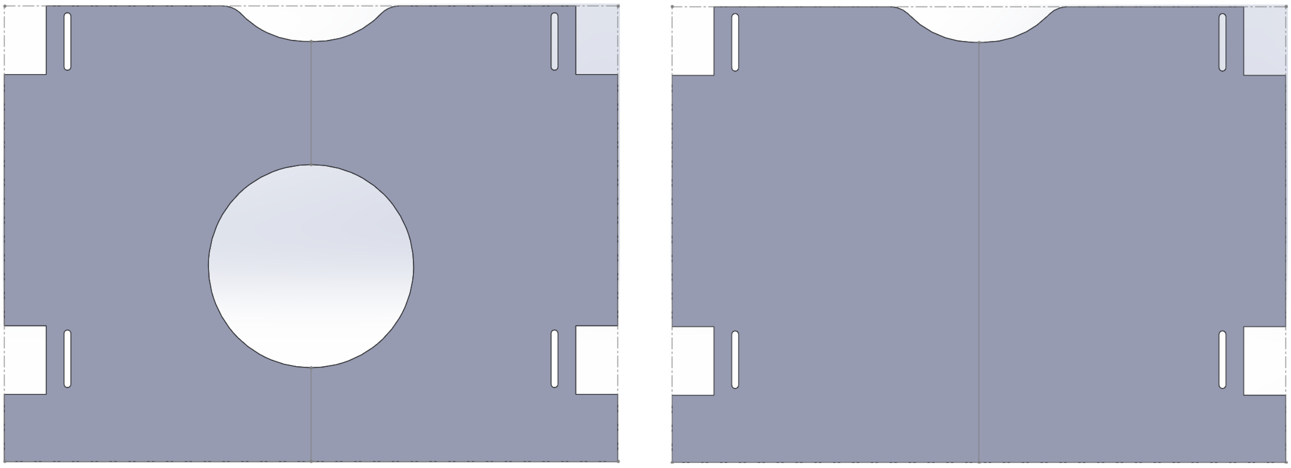

(c) back-side panel with window. **(d)** back-side panel without window.

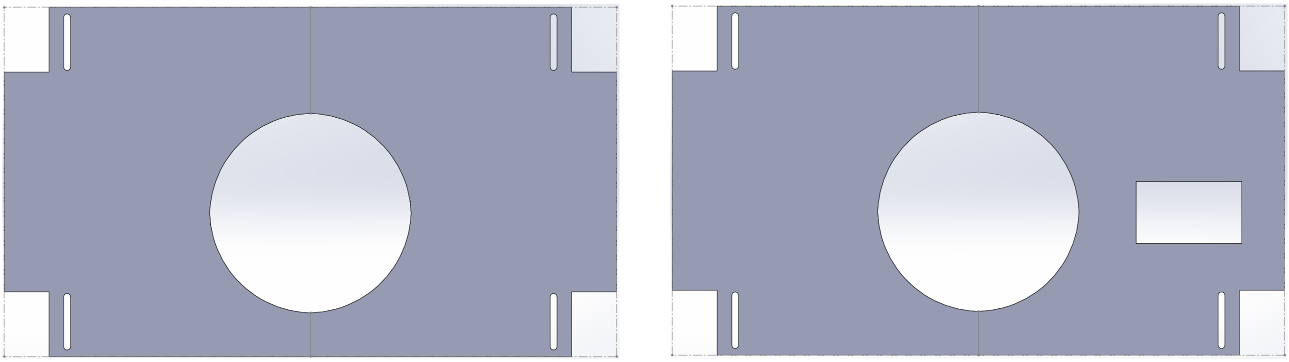

(e) Middle-side panel with window. **(f)** Middle-side panel with window and rail cutout.

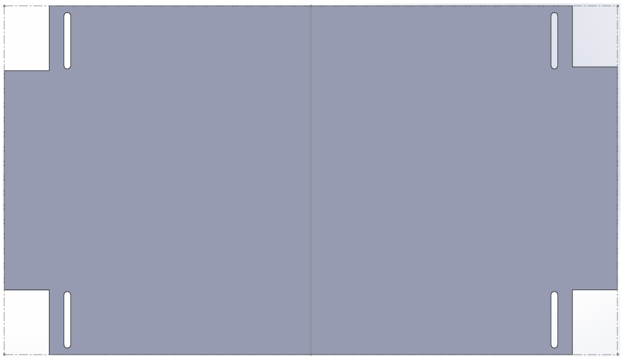

(g) Middle-side panel without window.

Figure 6.14 All variants of the aluminum sheet panels and their respective locations.

design variants. Similar to the ends of the chamber, one variant had a window opening while the other did not. The third variant had an additional cutout to accommodate the attachment points of the telescopic rails. This can be seen in subfigure 6.14f. The other sheet variants throughout the chamber can also be seen in Figure 6.14. These represent all the required sheets, a total of 12, for a single layer of shroud.

Table 6.2 Quantity and locations of thermal shroud aluminum sheet variants.

Sheet description	Location in chamber	# of sheets required	Figure reference
Front-side sheet with a window	Top and Sides	3	Figure 6.14a
Front-side sheet without a window	Bottom	1 (+1)	Figure 6.14b
Back-side sheet with a window	Top and Sides	3	Figure 6.14c
Back-side sheet without a window	Bottom	1 (+1)	Figure 6.14d
Middle sheet with window	Top	1	Figure 6.14e
Middle sheet with a window and cutout	Sides	2	Figure 6.14f
Middle sheet without window or cutout	Bottom	1 (+1)	Figure 6.14g
	Sum:	15	

Since the design require a second layer at the bottom, 3 additional sheets, that are without a window opening, are made to further shield the cold plate from radiation losses from underneath it, driving the total up to 15. Table 6.2 summarizes the number of sheets required from each variant as well as where said sheet would be located.

Since there exists only 4 attachment points along a row, but three instances of sheets along that row, there has to be some overlap in the sheets. The sheets are staggered to accommodate this overlap. First, the sheets at the middle of the chamber are placed, then following a Teflon spacer, the sheets on each end of the chamber are assembled. Figure 6.15 depicts this overlap and staggering of the layers. This is also beneficial when pressurizing or depressurizing the chamber as it allows for easier pathways for air to flow.

Since there would be an overlap between between layers, the location of the mounting slots on higher level sheets need to align perfectly with lower level layers and then the Teflon block underneath it. Assuming an offset or gap between the layers of 5 mm at which the Teflon spacers would be located, layers within the shroud would have nominal radii of 310, 305, 300, and 295 mm. The distance between the mounting slots and the edge next to it are therefore varied to ensure that when these sheets are bent into concentric arcs, all holes would align. In other words, the direct radial projection of the slot positions should be aligned so that all slots share the same angular position around a common center.

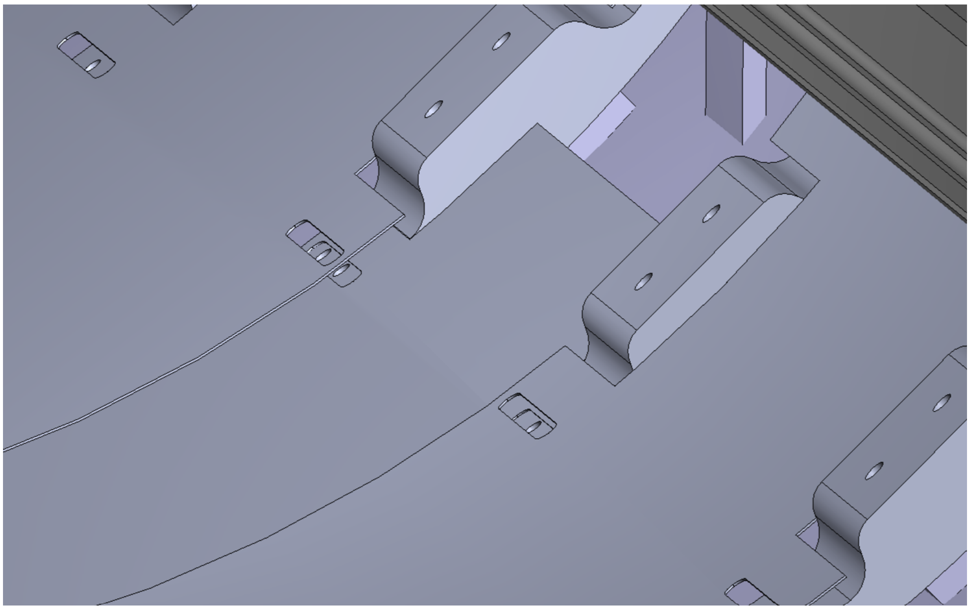

Figure 6.15 Staggering of the aluminum layers and alignment of mounting slots.

This geometric constraint is defined as follows. Let r_i denote the radius of the i-th layer, and let θ_k be the angular coordinate of the k-th mounting hole (measured from a fixed reference axis). The Cartesian coordinates of the hole on any layer are given by:

$$x_k^{(i)} = r_i \cos(\theta_k) \tag{6.3}$$

$$y_k^{(i)} = r_i \sin(\theta_k) \tag{6.4}$$

For perfect alignment, θ_k is calculated for the lowermost layer, then used along side varying radii to determine the Cartesian coordinates of the slots. In practice, this means the holes are located at the same angular intervals (e.g., every 90° for four holes), while their radial positions vary according to the layer radius. This calculation is the reason Figure 6.13 depicted the spacing between the slot and the edge next to it as varying.

6.6 Door Shroud

Finally, with the aluminum sheets shielding from radiation towards the chamber walls, there still remains radiation towards the doors of the chamber. The door shroud follows the same design language as the main structure and has the same requirements in terms of material selection, thermal decoupling and assembly. This design, however was vastly simpler. The new door shroud has the same shape as the previous shroud albeit with some minor differences.

First, the shroud is made slightly taller to cover more area towards the top of the chamber. This area additional area is a result of the new shroud providing more space for experimentation. Secondly, the shroud is now 2 mm thick as opposed to the original 5mm version. While the aluminum panels covering the sides of the chamber are 0.75 mm, the door shroud needs to be thicker to provide structural integrity to the platforms on the side of the cold plate. Thirdly, the shroud, of course, does not have tubes attached to it anymore, instead it is made from the same 1000-series alloy material as the rest of the aluminum sheets.

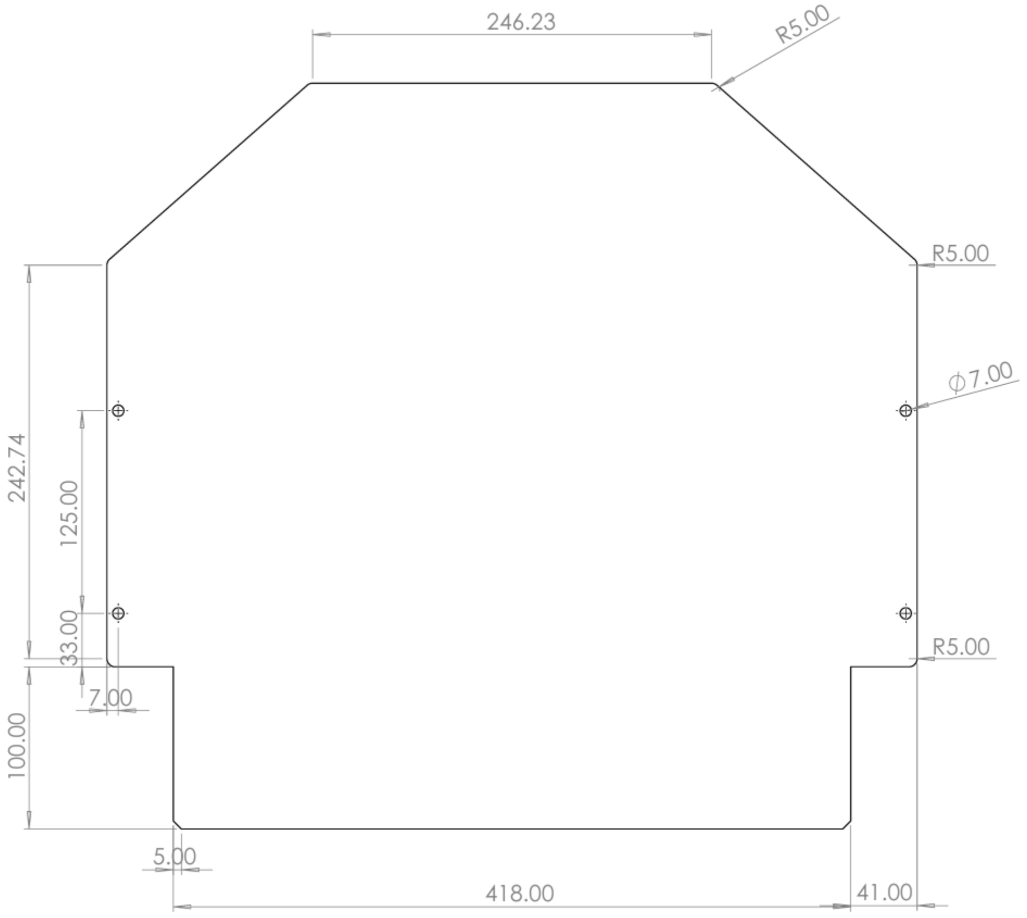

Figure 6.16 Updated door shroud geometry with mounting hole layout.

Figure 6.16 shows a drawing of the door shroud with relevant dimensions. It also shows 4 mounting holes, through which the shroud integrates with the cold plate. It mounts to a pair of 90° elbows. Thermal decoupling is achieved through the use of Teflon spacers. Figure 6.17 shows the shroud mounted to the rest of the cold plate and the space available for the Teflon spacers, while Figure 6.18 shows the full assembly of the door shrouds to the rest of the structures and cold plate.

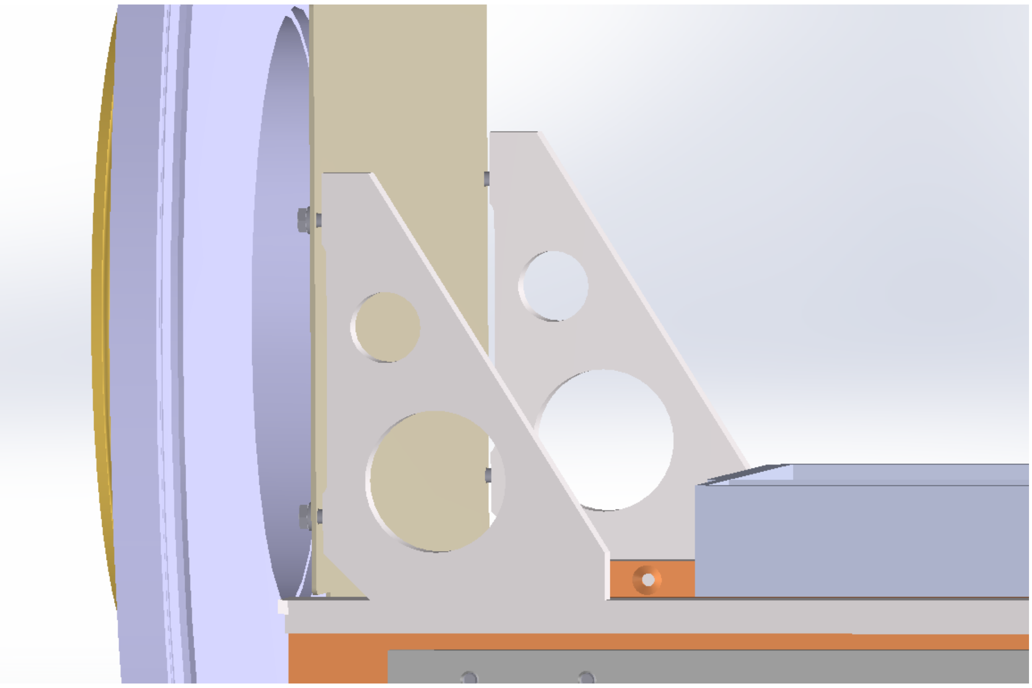

Figure 6.17 Mounting interface between door shroud and cold plate as seen from the side.

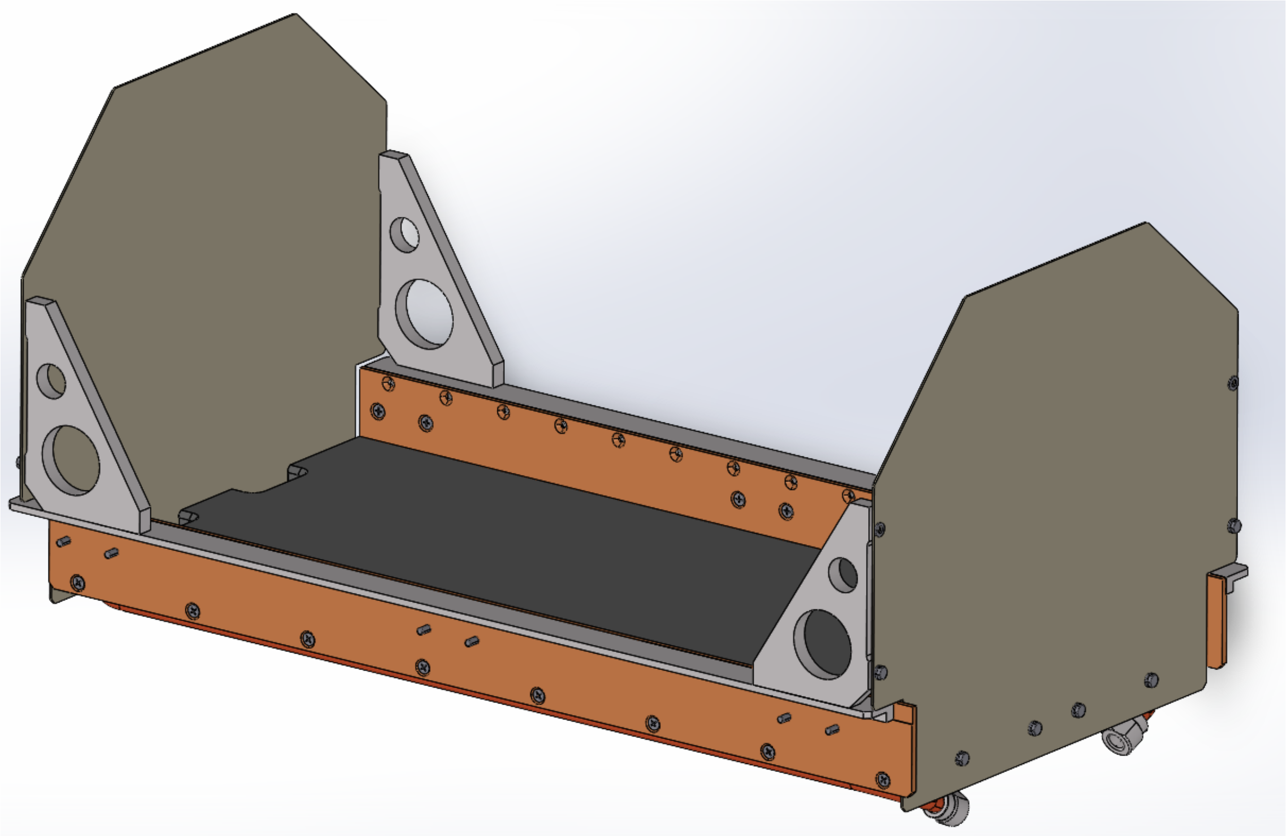

Figure 6.18 Final assembly of door shroud integrated with cold plate and side structures.

7 Conclusion

7.1 Summary

This work documented the evaluation and redesign of the thermal environment control system for the *LISA* thermal-vacuum chamber at the Technical University of Munich. The chamber, originally developed for the *LISA* project, has been repurposed for regolith-based experiments in a dirty vacuum environment.

After identifying a number limitations in the original cold plate and thermal shroud system—particularly excessive volume usage and leakage, a comprehensive redesign process was initiated. This involved defining new system requirements, simulating thermal performance under various shroud configurations, and integrating constraints derived from upcoming experiments, such as the Rover Permittivity Sensor (*RPS*) project.

The cold plate was assessed for replacement; however, due to budgetary limitations, the existing plate was retained. Still, alternative designs were evaluated and documented for potential future implementation. On the other hand, a new thermal shroud was developed from scratch, with a strong emphasis on minimizing radiative losses while maximizing usable space within the chamber. The final shroud design consists of a single full-body layer, made from several panels, and a second partial layer covering the lower half of the chamber, offering near-optimal thermal performance with minimal spatial compromise.

7.2 Limitations

While the final design fulfills the system-level requirements and offers tangible performance improvements, a few limitations remain. The thermal simulations used to inform design decisions were based on steady-state assumptions and simplified models. Initial attempts at transient, multiphysics simulations produced questionable results and were extremely time-consuming. Considering that a thermal simulation is not the main focus of this work, instead it is only a small part of it that was used for comparison of various shroud configurations, and so only steady-state simulations were presented.

Additionally, the retention of the original cold plate imposes performance limitations, particularly due to its exposed tubes on the lower side, which present significant radiative losses. While the current solution is workable, a full performance upgrade would still require a new vacuum-compatible cold plate and fluid interface system. The retention of the current plate applies significant pressure on the shroud subsystem to sufficiently shield the radiative losses, therefore this project practically tries to push the limits of passive cooling and shielding given the available resources.

7.3 Outlook

Despite the above limitations, this work establishes a robust and modular thermal control framework for future dusty vacuum experiments at *TUM*. The chamber is now equipped to accommodate experiments such as the *RPS* wheel test, with sufficient thermal insulation, accessibility, and expansion capability. Currently, most parts are either in manufacturing or being delivered and initial setup and integration are expected to begin shortly. Once integrated, the thermal performance will be evaluated and any improvements can be identified.

In the future, implementing a custom-designed vacuum brazed cold plate remains a viable upgrade. This should further reduce thermal gradients and improve system longevity. Similarly, enhancing simulation fidelity, through validated transient *COMSOL* models and improved boundary conditions, would provide a deeper understanding of transient effects and inform further improvements to both the cold plate and shroud. Overall, the results presented here demonstrate that meaningful performance improvements are possible within budgetary and mechanical constraints, and that passive cooling techniques, when combined with careful design, can yield thermally efficient and adaptable systems for planetary simulation environments.

Bibliography

3M (2022). 3m novec 7100 engineered fluid. `https://multimedia.3m.com/mws/media/1998180/3m-novec-7100-engineered-fluid.pdf?&fn=nvc7100.pdf`. Accessed: 2025-04-16.

Acedera, R. A. (2024). How outgassing in materials is tested: Key parameters and procedures. `https://blog.caplinq.com/how-outgassing-in-materials-is-tested-key-parameters-and-procedures_5209/`.

Amlinger, H. and Bosma, C. (1986). Thermal testing facilities for spacecraft systems. *ESA Journal*, 10(3):235–245.

Boyd Corporation (2025). Assessing the quality of a tubed cold plate. Accessed: 2025-04-16.

Brinkmann, K. (1984). Thermal test techniques for space systems. *ESA SP*, 201:37–46.

Crane Co. (2018). *Flow of Fluids Through Valves, Fittings, and Pipe (Technical Paper No. 410)*. Crane Co., Northbrook, IL, 29 edition.

Davis, J. R. (1993). *Aluminum and Aluminum Alloys*. ASM International, Materials Park, OH.

DuPont (n.d.). Vespel technical data. Available at `https://www.dupont.de/vespel.html`.

Edwards, A. (1992). Operational experiences from the large space simulator upgrade. *ESA Bulletin*, (71):215–222.

European Space Agency (2024). Large space simulator interior view. `https://www.esa.int/Enabling_Support/Space_Engineering_Technology/Test_centre/Large_Space_Simulator_LSS`. Image courtesy of ESA, accessed 2025-04-16.

Gilmore, D. G. (2002a). *Spacecraft Thermal Control Handbook: Volume I - Fundamental Technologies*. The Aerospace Press, El Segundo, CA.

Gilmore, D. G. (2002b). *Spacecraft Thermal Control Handbook: Volume II - Cryogenics*. The Aerospace Press, El Segundo, CA.

Haefer, R. (1972). *Vacuum Technology in Space Research*. Springer-Verlag.

Holkeboer, J., Ellis, W., and Guy, A. (1966). Thermal test simulation of the outer space environment. Technical Report NASA-TN-D-3665, NASA.

Huber Kältemaschinenbau AG (2023). Unistat 1015w - technical data sheet. `https://www.huber-online.com/daisy_website_files/datenblaetter/en/1064.0002.01.PDF`. Accessed: 2025-04-16.

Incropera, F. P., DeWitt, D. P., Bergman, T. L., and Lavine, A. S. (2007). *Fundamentals of Heat and Mass Transfer*. John Wiley & Sons, 6th edition.

International Organization for Standardization (2011). Iso 3529-1:2011 – vacuum technology – vocabulary – part 1: General terms. Retrieved from `https://cdn.standards.iteh.ai/samples/73312/c216a7d729c14909ab4fa9e81d992c6d/ISO-3529-1-2019.pdf`.

Jousten, K. (2018). *Handbook of Vacuum Technology*. Wiley-VCH, 2nd edition.

Khan, M. and Fartaj, A. (2011). A review on microchannel heat exchangers and potential applications. *International Journal of Energy Research*, 35:553–582.

MatWeb, LLC (n.d.a). Overview of materials for 1000 series aluminum. Available at `https://www.matweb.com/search/DataSheet.aspx?MatGUID=38e1c167c7ea4dfebf80778b29ae71cf`.

MatWeb, LLC (n.d.b). Overview of materials for 2000 series aluminum. Available at `https://www.matweb.com/search/DataSheet.aspx?MatGUID=2076184469d740af9f86b0d69b2e42ff`.

MatWeb, LLC (n.d.c). Overview of materials for 5000 series aluminum. Available at `https://www.matweb.com/search/DataSheet.aspx?MatGUID=c71186d128cd423d9c6d51106c015e8f`.

MatWeb, LLC (n.d.d). Overview of materials for 6000 series aluminum. Available at `https://www.matweb.com/search/DataSheet.aspx?MatGUID=26d19f2d20654a489aefc0d9c247cebf`.

Mersen (2024). Aquamax® vacuum brazed cold plates. `https://www.mersen.com/en/products/cooling-solutions/aquamaxr-vacuum-brazed-cold-plates`. Accessed: 2025-04-16.

Modest, M. F. (2013). *Radiative Heat Transfer*. Academic Press, 3rd edition.

O'Hanlon, J. F. (2003). *A User's Guide to Vacuum Technology*. Wiley-Interscience, 3rd edition.

Puretecs GmbH (2023). Hfe-7100 mixture – technical data sheet. `https://www.puretecs.de/images/pdf-en/cooling/tds%20of%20HFE-7100%20mixture%20PT.pdf`. Accessed: 2025-04-16.

Rollon GmbH (2024). Hvc linear actuator – technical data. `https://my.rollon.com/de/en/product/hvc/?page&post_type=product&lang=en#technical-data`. Accessed: 2025-04-16.

Shah, R. K. and Sekulic, D. P. (2003). *Heat Exchanger Pressure Drop Analysis*, chapter 6, pages 378–424. John Wiley & Sons.

Umrath, W. (2016). *Fundamentals of Vacuum Technology*. Pfeiffer Vacuum GmbH, 5th edition.

Victrex Plc (n.d.). Peek polymer properties. Available at `https://www.victrex.com/de/products/polymers/peek-polymers`.

A COMSOL Contours

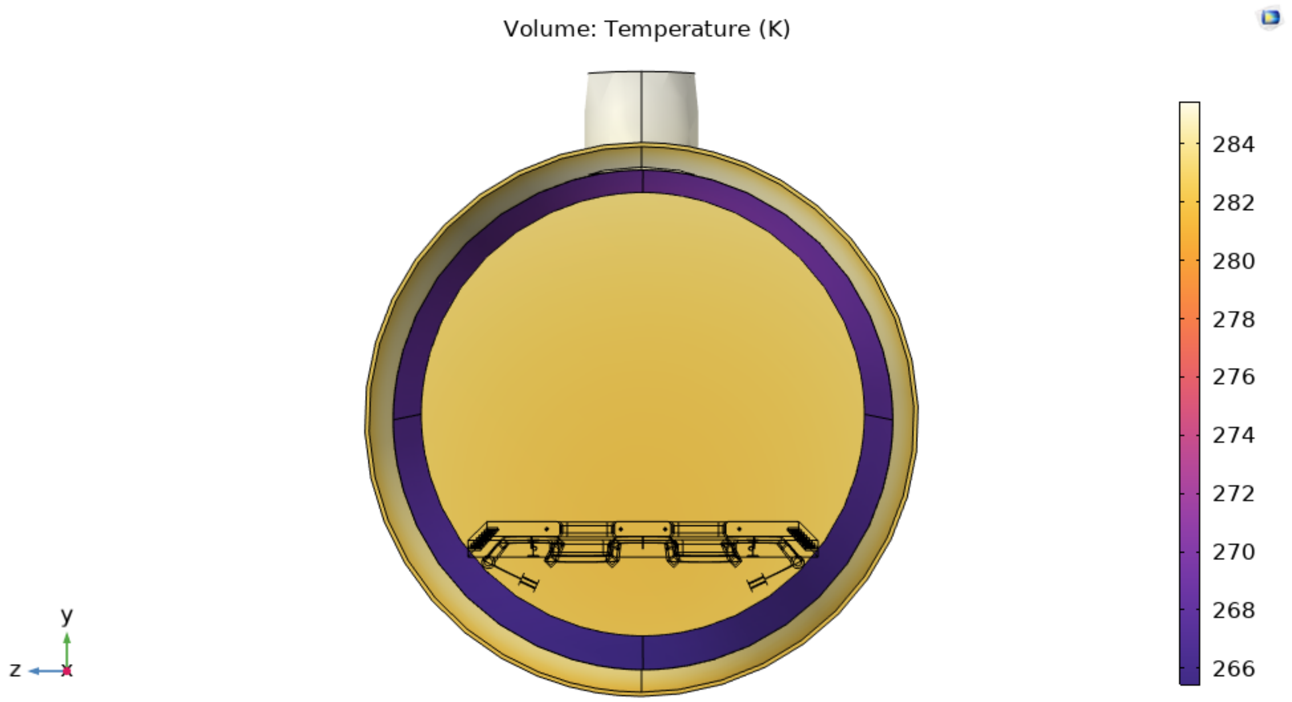

Figure A.1 Re-scaled temperature contours of a steady-state simulation involving the chamber, cold plate and a single layer of shroud.

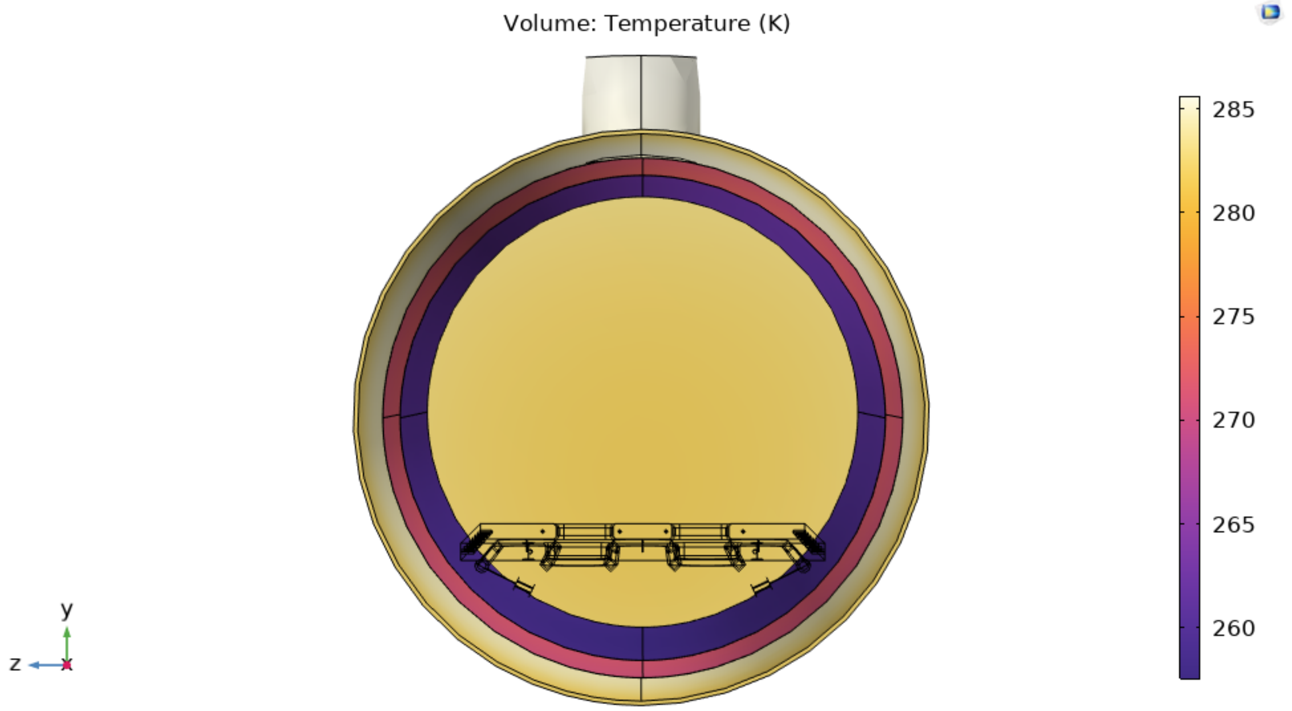

Figure A.2 Re-scaled temperature contours of a steady-state simulation involving the chamber, cold plate and a double layer of shroud.

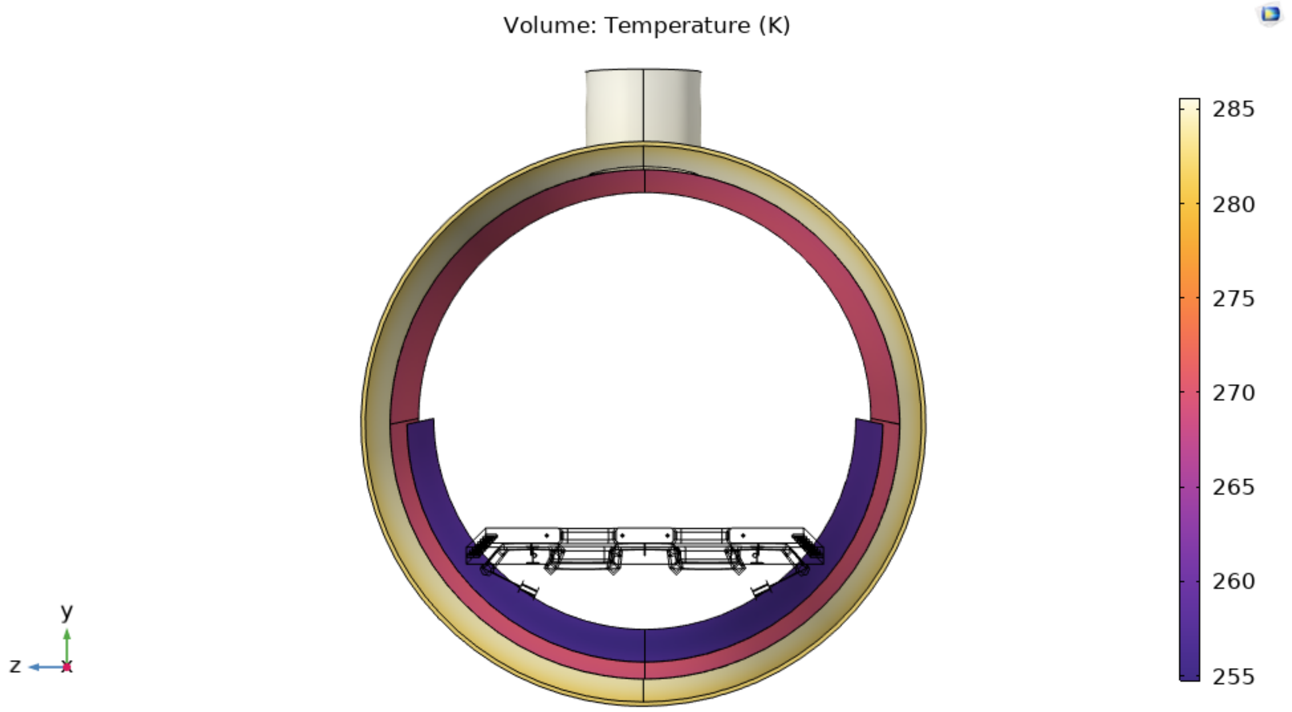

Figure A.3 Re-scaled temperature contours of a steady-state simulation involving the chamber, cold plate and 1.5 layers of shroud.

B TVAC Internal Photos

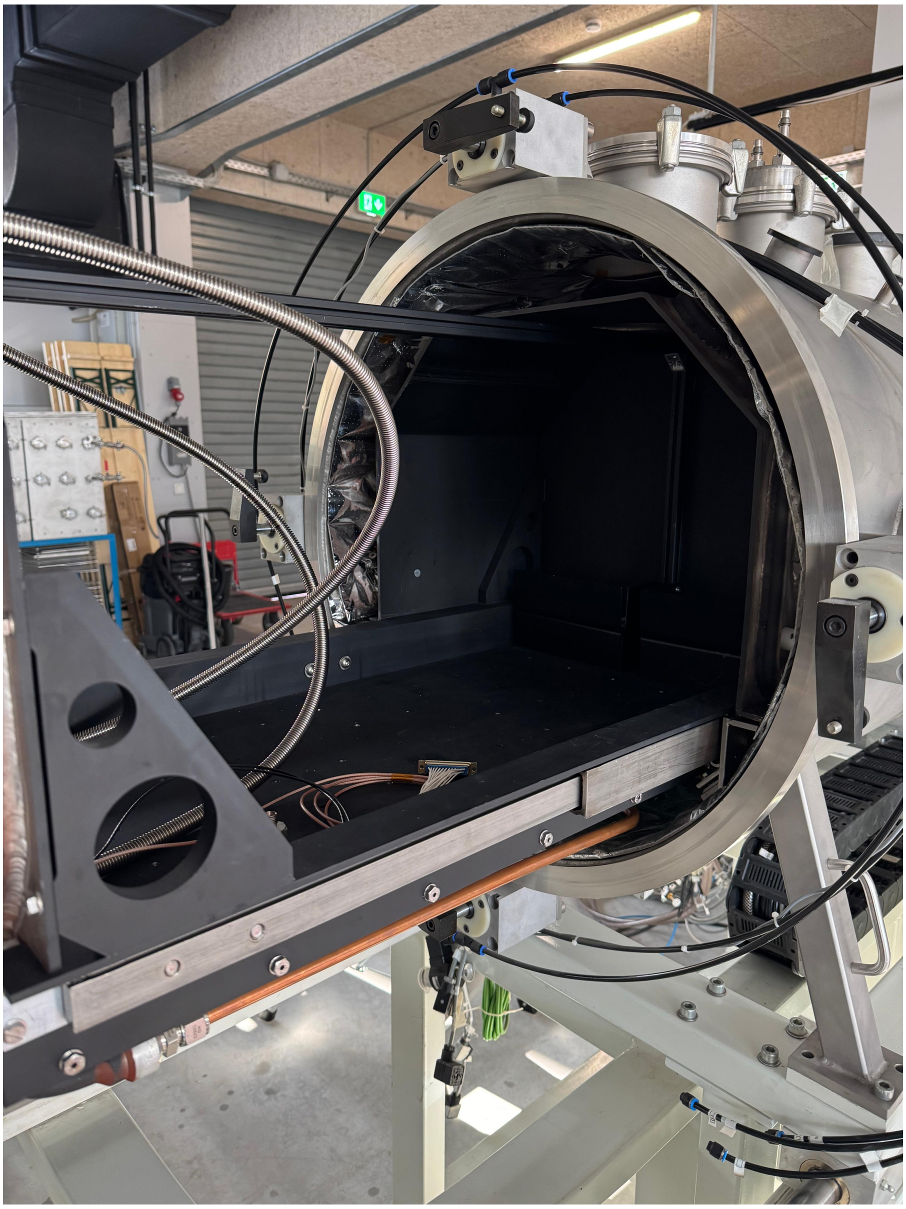

Figure B.1 The previous shroud with a gantry system mounted on the inside. The Old MLI can also be seen.

Figure B.2 A close-up of the attachment point depicting some contamination from previous shroud system as well.

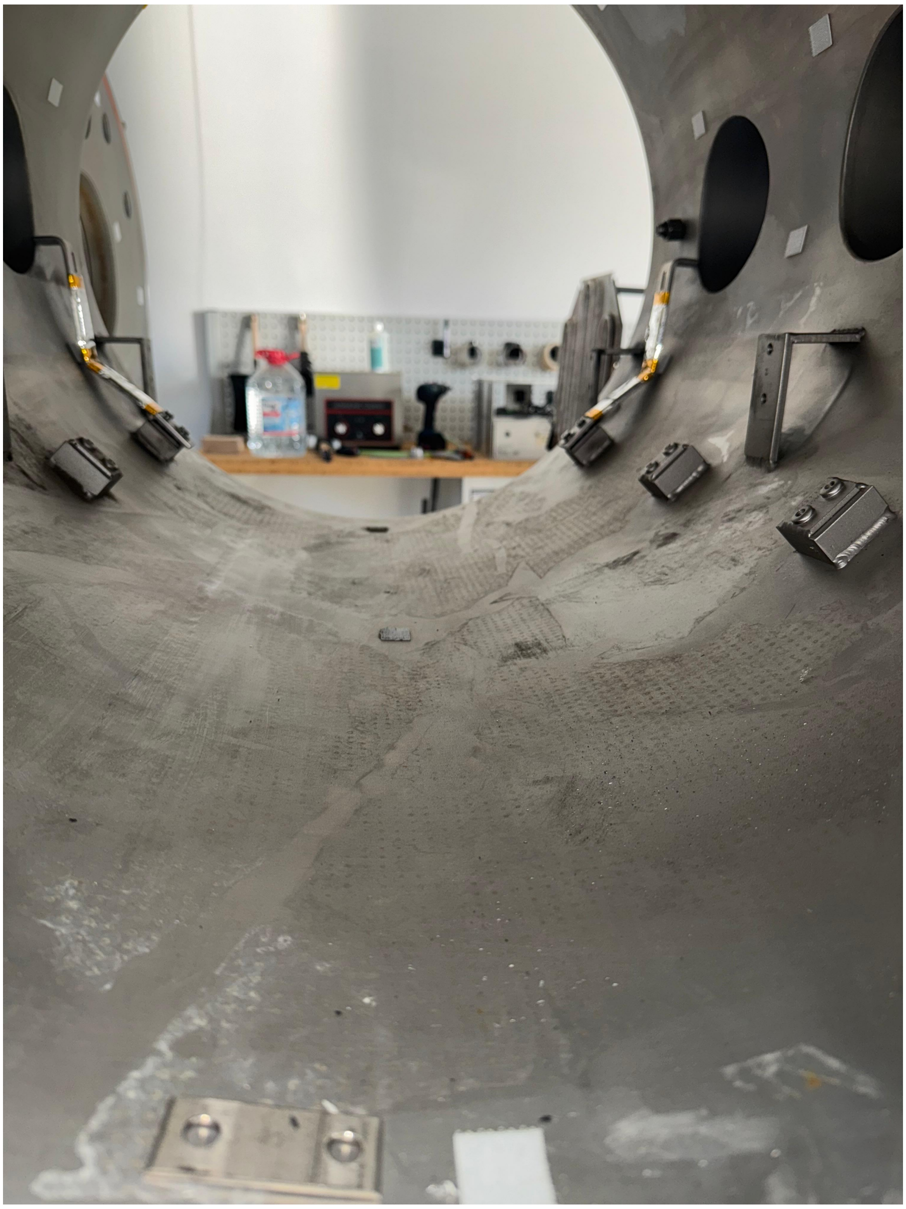

Figure B.3 Contamination inside the chamber encountered during the cleaning of the chamber.

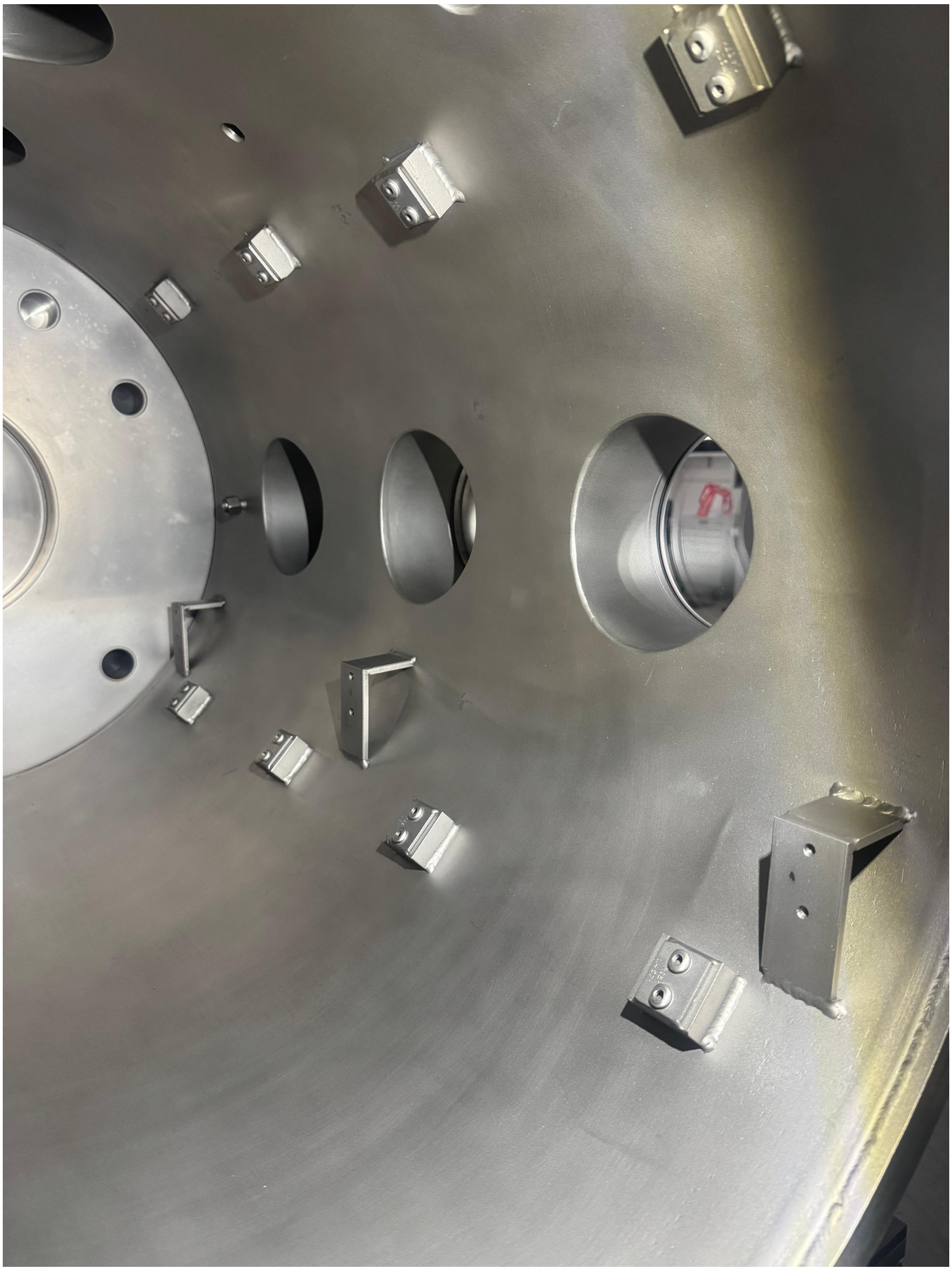

Figure B.4 A wide-view of the attachment points and rail mounting interface.

C Teflon Adapter Block Drawings

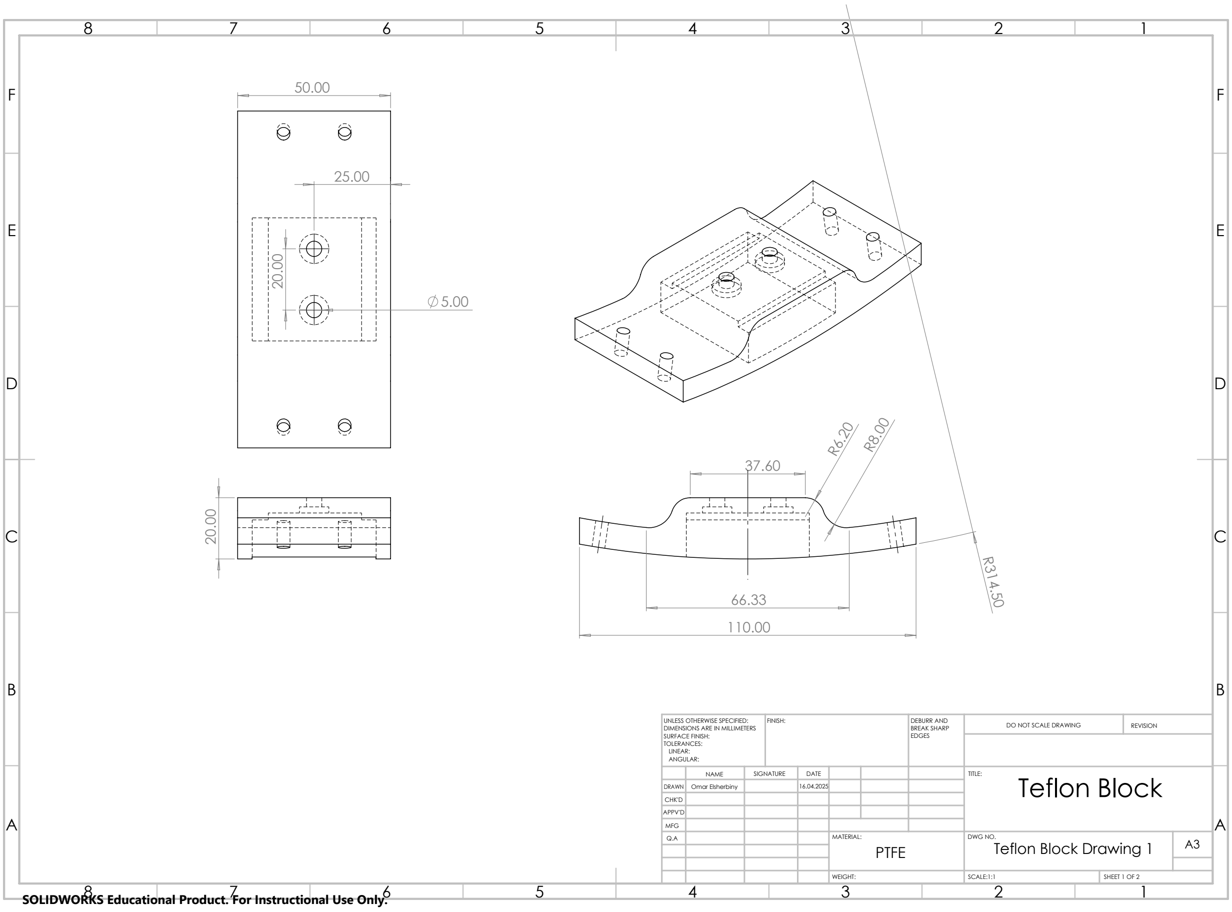

Figure C.1 Dimensional drawing of the teflon adapter block.

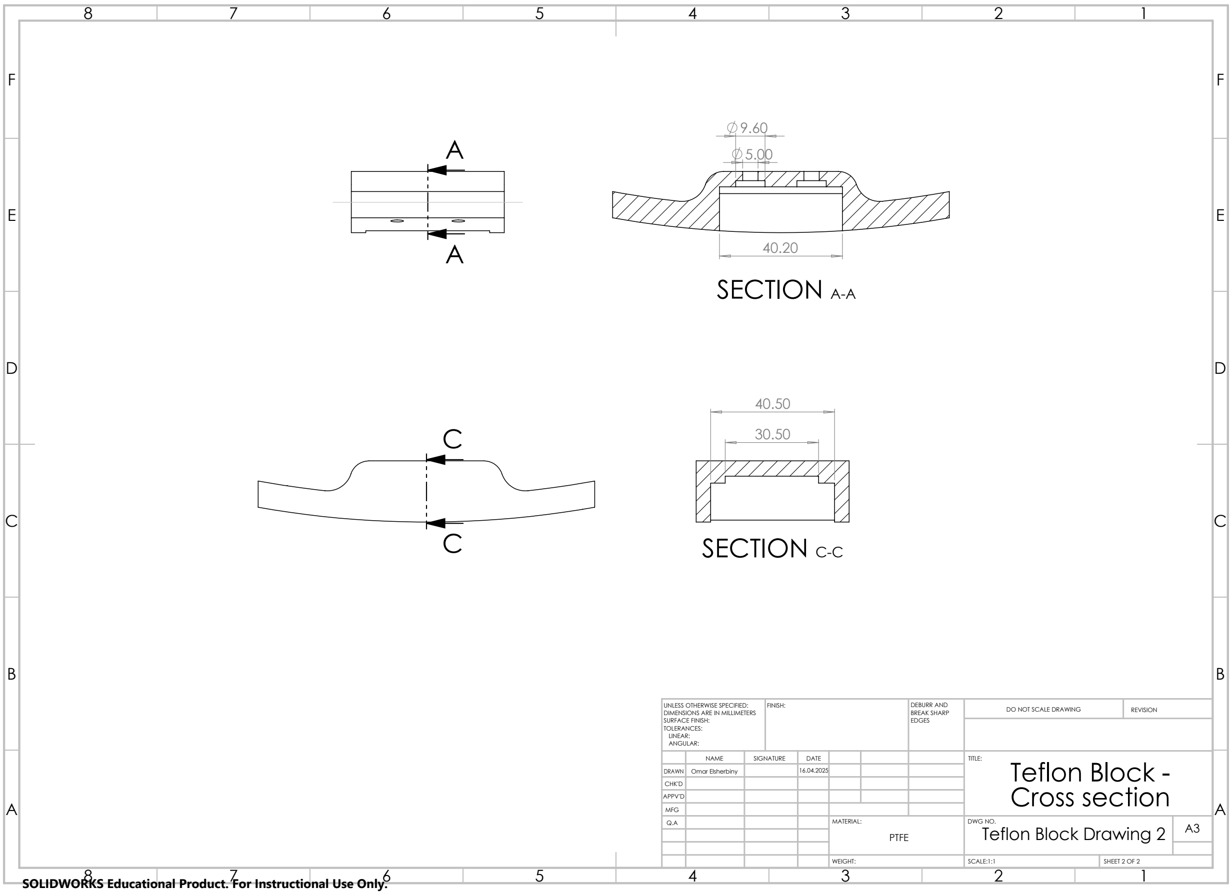

UNLESS OTHERWISE SPECIFIED:
DIMENSIONS ARE IN MILLIMETERS
SURFACE FINISH:
TOLERANCES:
LINEAR:
ANGULAR:

FINISH:

DEBURR AND BREAK SHARP EDGES

DO NOT SCALE DRAWING

REVISION

	NAME	SIGNATURE	DATE
DRAWN	Omar Elsherbiny		16.04.2025
CHK'D			
APPV'D			
MFG			
Q.A			

TITLE: Teflon Block - Cross section

MATERIAL: PTFE

DWG NO. Teflon Block Drawing 2

A3

WEIGHT:

SCALE:1:1

SHEET 2 OF 2

Figure C.2 Dimensioned section-view of the teflon adapter block

D Material Properties

Table D.1 Comparison of High-Performance Polymers for Thermal and Manufacturing Considerations

Property	**Teflon (PTFE)**	**Vespel**	**PEEK**
Thermal Properties			
Thermal Conductivity [W/m·K]	0.25 (**?**)	0.35 (DuPont, nd)	0.25–0.30 (Victrex Plc, nd)
Thermal Diffusivity [mm^2/s]	$\sim$0.13	$\sim$0.18	$\sim$0.17
Max Continuous Use Temp [℃]	260 (**?**)	300+ (DuPont, nd)	250–260 (Victrex Plc, nd)
Manufacturability			
Machinability	Excellent	Excellent	Good
Formability	Poor	Not Formable (machined)	Good
Weldability/Bonding	Difficult	Possible (adhesives)	Moderate
Availability and Cost			
Availability	High	Moderate (special order)	High
Cost	Low	Very High	High

	6000 Series	5000 Series	2000 Series	1000 Series
Vacuum Fitness				
Vapor Pressure	Sufficiently Low (Davis, 1993)			
Outgassing Rate	Sufficiently Low (Davis, 1993)			
Mechanical Properties				
Yield Strength [MN/m^2]	283 (MatWeb, LLC, ndd)	239 (MatWeb, LLC, ndc)	309 (MatWeb, LLC, ndb)	68.9 (MatWeb, LLC, nda)
Modulus of Elasticity [GN/m^2]	83.2 (MatWeb, LLC, ndd)	70.3 (MatWeb, LLC, ndc)	76.3 (MatWeb, LLC, ndb)	68.5 (MatWeb, LLC, nda)
Density [kg/m^3]	2710 (MatWeb, LLC, ndd)	2630–2840 (MatWeb, LLC, ndc)	2790 (MatWeb, LLC, ndb)	2700 (MatWeb, LLC, nda)
Thermal Properties				
Specific Heat Capacity [J/(kg K)]	900 (**?**)	900 (**?**)	875 (**?**)	900 (**?**)
Thermal Conductivity [W/(m K)]	166 (**?**)	121–152 (**?**)	120 (**?**)	235 (**?**)
Thermal Deformation [µm/(m K)]	23 (**?**)	24 (**?**)	22.5 (**?**)	24 (**?**)
Calc. Thermal Diffusivity [mm^2/s]	$\sim$63 [calc.]	$\sim$55 [calc.]	$\sim$50 [calc.]	$\sim$90 [calc.]
Chemical Resistance				
	Good (Davis, 1993)	Excellent (marine-grade) (Davis, 1993)	Poor (corrosion-prone) (Davis, 1993)	Excellent (Davis, 1993)
Manufacturability				
Cutting	Easy	Easy	Moderate	Easy
Forming	Moderate	Easy	Difficult	Easy
Joining	Moderate	Good	Difficult	Easy
Availability				
Availability	High	High	Moderate	High
Cost	Low	Low	High	Low
Conclusion				
	All-purpose alloy	Best corrosion resistance	Aerospace-grade, high strength	Best conductivity, soft

Table D.2 Comparison of Aluminum Alloy Series for Thermal Shroud Applications